Elys deficiency constrains Kras-driven tumour burden by amplifying oncogenic stress

Kimberly J Morgan[1,2], Karen Doggett[1,2], Fan-Suo Geng[1,3], Lachlan Whitehead[2,4], Kelly A Smith[5,6], Benjamin M Hogan[6,7], Cas Simons[6,8], Gregory J Baillie[6], Ramyar Molania[2,9], Anthony T Papenfuss[2,9], Thomas E Hall[6], Elke A Ober[10], Didier Y R Stainier[11], Zhiyuan Gong[12] and Joan K Heath[1,2,*]

[1]Epigenetics and Development Division, Walter and Eliza Hall Institute of Medical Research, Parkville, Victoria 3052, Australia

[2]Department of Medical Biology, University of Melbourne, Parkville, Victoria 3010, Australia

[3]Genomics and Epigenetics Division, Garvan Institute of Medical Research, Darlinghurst, New South Wales, Australia and St Vincent's Clinical School, Faculty of Medicine, University of New South Wales, New South Wales 2010, Australia

[4]Centre for Dynamic Imaging, Advanced Technology and Biology Division, Walter and Eliza Hall Institute of Medical Research, Parkville, Victoria 3052, Australia

[5]Department of Physiology, The University of Melbourne, Parkville, Victoria 3010, Australia

[6]Institute for Molecular Biosciences, The University of Queensland, Brisbane, Queensland 4072, Australia

[7]Peter MacCallum Cancer Centre, Melbourne, Victoria 3000, Australia

[8]Murdoch Children's Research Institute, Parkville, Victoria 3052, Australia

[9]Bioinformatics Division, Walter and Eliza Hall Institute of Medical Research, Parkville, Victoria 3052, Australia

[10]Danish Stem Cell Center, University of Copenhagen, 2200 Copenhagen N, Denmark

23 [11]Max Planck Institute for Heart and Lung Research, Dept. III – Developmental Genetics

24 Ludwigstrasse 43, 61231 Bad Nauheim, Germany

25 [12]Department of Biological Science, National University of Singapore, Singapore

26 ***Corresponding Author:** Joan K Heath, Walter and Eliza Hall Institute of Medical Research, 1G Royal

27 Parade, Parkville, Victoria 3052, Australia. Phone: (+613) 9345-2872

28 Email: joan.heath@wehi.edu.au

29 **Declaration of interests**: The authors declare no potential conflicts of interest

30

ABSTRACT

The nucleoporin ELYS, encoded by *AHCTF1*, is a large multifunctional protein with essential roles in nuclear pore assembly and mitosis. Using a zebrafish model of hepatocellular carcinoma, in which the expression of an inducible mutant *kras* transgene *(kras^{G12V})* drives hepatocyte-specific hyperplasia and liver enlargement, we show that reducing *ahctf1* gene dosage by 50% markedly shrinks tumour burden, while non-hyperplastic tissues are unaffected. We demonstrate that *ahctf1* heterozygosity impairs nuclear pore formation, mitotic spindle assembly and chromosome segregation, leading to DNA damage and activation of TP53-dependent and independent mechanisms of cell death and cell cycle arrest. This selective vulnerability of cancer cells to mild disruption of Elys function uncovers a novel synthetic lethal interaction between *ahctf1* and *kras* mutations that could be exploited therapeutically. Heterozygous expression of both *ahctf1* and *ranbp2*, or treatment of heterozygous *ahctf1* larvae with the nucleocytoplasmic transport inhibitor, Selinexor, completely blocked *kras^{G12V}*-driven hepatocyte hyperplasia, revealing promising avenues for combinatorial treatments.

44 **INTRODUCTION**

45 Synthetic lethality is the term used to describe the death of cells in response to co-existing disruptions
46 in two different genes, neither of which is lethal alone. The phenomenon has emerged as a promising
47 tool for cancer drug development[1]. The advantage of the approach lies in its capacity to induce the
48 death of a vulnerable cell population, such as oncogene-expressing cancer cells, while healthy cells
49 are unaffected. The approach has been validated in the clinic by the use of poly(adenosine
50 diphosphate [ADP]-ribose) polymerase (PARP) inhibitors to treat tumours carrying mutations in the
51 breast cancer susceptibility genes, *BRCA1*/*BRAC2*[2], and its success has fuelled the search for other
52 clinically relevant pairwise combinations. Particular effort has been directed towards identifying genes
53 whose partial loss of function confers synthetic lethality in cancer cells containing hitherto
54 'undruggable' oncogene targets, such as mutant *KRAS*[3,4]. In this paradigm, the interacting gene is not
55 mutated in cancer nor oncogenic in its own right; however, its function is essential to maintain the
56 tumourigenic state, inspiring the concept of non-oncogene addiction[5].

57 In this paper, we tested whether *AHCTF1* exhibits the properties of a mutant *KRAS* synthetic lethal
58 interacting gene. *AHCTF1* encodes ELYS, a 252 kDa multidomain nucleoporin that was first discovered
59 in mouse development where it was shown to be required for the proliferation and survival of inner
60 mass cells[6]. Since then, ELYS has been studied in many model systems, including in a zebrafish
61 development mutant (ti262)[7], where we and others showed that homozygous inheritance of an ENU-
62 induced nonsense mutation in *ahctf1* disrupted nuclear pore formation and caused catastrophic levels
63 of cell death in highly proliferative cell compartments, such as the intestinal epithelium, while
64 relatively quiescent tissues survived and remained healthy[8,9].

65 As well as being a structural component of nuclear pore complexes (NPCs), ELYS is essential for their
66 formation at the end of mitosis[10-12]. NPCs are huge (110 MDa) multi-subunit complexes comprising at
67 least 30 different nucleoporins (Nups) in an octameric array[13]. They form cylindrical channels in the
68 nuclear envelope (NE) and regulate nucleocytoplasmic transport and intracellular localisation of large

69 (>40 kDa) molecules. In the absence of ELYS, the NE is re-built at the end of mitosis, but this occurs
70 without NPC formation, precluding mRNAs and many proteins from moving in and out of the nucleus.
71 By providing a platform for NPC re-assembly at the end of mitosis (Fig. 1a,b), ELYS restores
72 nucleocytoplasmic trafficking, and thereby facilitates entry into the nucleus of proteins such as G1 and
73 S phase cyclin-dependent kinases that are required for DNA replication and cell cycle progression (Fig.
74 1c). Also in G1/S phase, ELYS regulates transcription and DNA replication by reversible binding to
75 components of the SWI/SNF 80 chromatin remodeller complex, PBAP, and the DNA replication origin
76 licensing system, MCM2-7, respectively (Fig. 1d-f)[11,12,14,15].

77 At the end of G2, the cell has grown to a critical size and is prepared for M phase (Fig. 1g). The NE
78 breaks down (NEBD) and NPCs are disassembled (Fig. 1h). Whereas most Nups disperse throughout
79 the cytoplasm and the endoplasmic reticulum (ER)[16,17], ELYS, together with components of the
80 Nup107-160 complex and RANBP2, play an important role in prophase by binding to the kinetochores
81 of recently replicated sister chromatids where they contribute to microtubule recruitment and spindle
82 assembly (Fig. 1i)[18-20]. At telophase, when the chromatids are fully separated, the spindle and
83 kinetochores dissolve and ELYS becomes tethered to thousands of sites on chromatin through its C-
84 terminal chromatin binding region where it promotes chromatin decondensation[15,21]. In G1, the N-
85 terminal half of ELYS provides a scaffold to bind the Nup107-160 complex and other ER-associated
86 Nups, thereby coupling the initiation of NPC assembly with euchromatin formation, restoration of
87 nucleocytoplasmic transport and transcription[11,22,23] and completing the cycle depicted in Fig. 1.

88 Given this diversity of functions throughout the cell cycle, it is not surprising that ELYS is an Achilles'
89 heel of highly proliferative cells[8,9], and this prompted us to ask whether this vulnerability extrapolates
90 to cancer cells *in vivo*. To do this, we employed a highly tractable zebrafish model of hepatocellular
91 carcinoma (HCC) in which hepatocyte hyperplasia and liver enlargement are driven by an inducible,
92 hepatocyte-specific *EGFP-kras*^{G12V} transgene[24]. In this study, we used two-photon microscopy to
93 accurately quantitate liver volume in the presence and absence of a single nonsense mutation in one
94 allele of the *ahctf1* locus[8,9]. Remarkably, we observed a pronounced reduction in tumour burden in

95 response to this mild (50%) reduction in *ahctf1* gene dosage, while the rest of the animal was
96 unaffected. We further show that this selective vulnerability of oncogenic *kras*^{G12V}-expressing liver
97 cancer cells to *ahctf1* heterozygosity possesses the hallmarks of a synthetic lethal interaction that may
98 be exploited therapeutically.

99 **RESULTS**

100 ***ahctf1* heterozygosity reduces tumour burden in a zebrafish *kras*^{G12V}-driven model of hepatocellular**
101 **carcinoma**

102 In the zebrafish *kras*^{G12V}-driven HCC model, the doxycycline-induced expression of a single *EGFP-*
103 *kras*^{G12V} transgene (genotype denoted *TO(kras*^{G12V}*)*$^{T/+}$) between 2-7 days post-fertilisation (dpf) leads
104 to the accumulation of a constitutively active, EGFP-tagged oncogenic form of Kras specifically in
105 hepatocytes[24] (Fig. 2a). This forced expression of *EGFP-kras*^{G12V} causes hepatocyte hyperplasia and a
106 substantial increase in liver volume that can be quantified by two-photon microscopy. To investigate
107 the requirement for Elys in this cancer setting, we introduced a mutant *ahctf1* allele (containing a
108 nonsense mutation at codon 1319) from a zebrafish development mutant (*flo*^{ti262})[7] into the genome
109 of this model. This resulted in a 57% reduction in *ahctf1* mRNA expression in *ahctf1*$^{+/-}$ larvae at 7 dpf
110 (Fig. 2b), indicating that the premature codon encoded by the nonsense mutation triggers nonsense
111 mediated decay rather than expression of a truncated Elys protein.

112 To determine the effect of *ahctf1* heterozygosity (and other treatments) on normal liver cells, we used
113 a control transgenic line, denoted *2-CLiP* (2-Colour Liver Pancreas), in which hepatocytes express
114 dsRed fluorescence but no oncogenic transgene[25]. Mean liver volume in this model at 7 dpf was 1.95
115 x 10^6 ± 4.99 x 10^4 μm^3 and did not change in response to *ahctf1* heterozygosity (Fig. 2c,d), consistent
116 with previous observations that *ahctf1* heterozygotes develop normally, reach sexual maturity, and
117 exhibit a normal lifespan[9]. In the *TO(kras*^{G12V}*)*$^{T/+}$ model, induced expression of oncogenic Kras^{G12V} leads
118 to hepatocyte hyperplasia and a striking (4.1-fold) increase in liver volume to 7.97 x 10^6 ± 1.21 x 10^5
119 μm^3, an increment of 6.02 x 10^6 μm^3 over the course of 5 d of dox treatment. Remarkably, the potency

120 of this strong oncogenic *kras*^{G12V} signal was pared back by *ahctf1* heterozygosity (down to 5.92 x 10^6 ±
121 8.83 x 10^4 µm^3), equating to a 35% reduction in excess liver volume. These data demonstrate that a
122 50% reduction in *ahctf1* gene dosage markedly restricts tumour burden in livers expressing oncogenic
123 *kras*^{G12V}, while having no effect on normal livers. Thus, mildly disrupted *ahctf1* expression is a selective
124 vulnerability of cancer cells.

125 Robust and persistent overexpression of RAS oncoproteins is frequently associated with oncogene-
126 induced stress comprising defects in DNA replication, DNA damage and genome instability. In the
127 presence of wildtype TP53, this damage is limited by activation of TP53 transcription pathways that
128 induce cell cycle arrest, senescence and apoptosis. To determine whether expression of *kras*^{G12V}
129 causes oncogene-induced stress and Tp53 activation in our model, we measured the levels of Tp53
130 protein in pooled lysates of micro-dissected *TO(kras*^{G12V}*)*$^{+/+}$ and *TO(kras*^{G12V}*)*$^{T/+}$ livers and the remains
131 of the larvae (Fig. 2e,f). No Tp53 signal was obtained from non-*kras*^{G12V}-expressing livers or the body
132 remains after liver removal. We detected a weak Tp53 signal in extracts of *ahctf1*$^{+/+}$*;TO(kras*^{G12V}*)*$^{T/+}$
133 livers, indicating that expression of the *kras*^{G12V} oncogene alone elicited a weak Tp53 response. In
134 contrast, a much stronger Tp53 signal (>3.5-fold) was detected in *ahctf1*$^{+/-}$*;TO(kras*^{G12V}*)*$^{T/+}$ livers,
135 demonstrating a more severe level of stress in heterozygous *ahctf1* hepatocytes expressing oncogenic
136 *kras*^{G12V} than occurs in hepatocytes that are WT for *ahctf1.*

137 **Loss of Tp53 function enhances *kras*^{G12V}-driven liver enlargement, which is partially alleviated by**
138 ***ahctf1* heterozygosity**

139 To test whether activation of the Tp53 pathway was involved in reducing the volume of *kras*^{G12V}-
140 expressing livers on a heterozygous *ahctf1* background, we repeated the experiment in the absence
141 of Tp53 function. Here, we utilised the zebrafish *tp53*^{e7} or *tp53*^{M214K} allele, which changes a conserved
142 amino acid residue within the Tp53 DNA-binding domain corresponding to a mutational hotspot in
143 human cancer, producing a transactivation-dead Tp53 variant[26]. Abrogating Tp53 function by
144 homozygous expression of this allele (denoted *tp53*$^{m/m}$) in *ahctf1*$^{+/+}$*;TO(kras*^{G12V}*)*$^{T/+}$ larvae supported a

145 further large increase (82%) in liver volume (1.25 x 10^7 ± 1.10 x 10^5 μm^3) compared to livers on the
146 *tp53*$^{+/+}$ background (Fig. 2g,h) (Supplementary Fig. 1-3), demonstrating that Tp53 function normally
147 restrains tumour growth and liver enlargement in this model. Interestingly, the increase in liver
148 volume was significantly blunted (35% reduction) on a heterozygous *ahctf1* background, despite the
149 absence of functional Tp53.

150 ***ahctf1* heterozygosity triggers cell death in *TO(kras*^{G12V}*)*$^{T/+}$ hepatocytes through Tp53-dependent and**
151 **independent mechanisms**

152 We previously showed that Tp53 protein was upregulated in the livers of *(kras*^{G12V}*)*$^{T/+}$ larvae on a
153 heterozygous *ahctf1* background (Fig. 2e). To determine whether this activated a Tp53-dependent cell
154 death response, we utilised a transgenic line, Tg(*actb2:SEC-Hsa.ANXA5-mKate2,cryaa:mCherry*)^{uq24rp}
155 (hereafter denoted *Annexin 5-mKate*) that constitutively expresses a fusion protein comprising
156 Annexin 5 and the far-red fluorophore mKate[27]. This fusion protein gives rise to discrete fluorescent
157 puncta in cells undergoing apoptosis by binding to phosphatidylserine that is normally inaccessible on
158 the inner leaflet of the plasma membrane but is exposed as the membrane breaks down.

159 Annexin 5 fluorescent puncta were sparsely distributed (1.5 puncta per 10^{-5} μm^3) throughout the livers
160 of *ahctf1*$^{+/+}$*;tp53*$^{+/+}$*;TO(kras*^{G12V}*)*$^{T/+}$ larvae demonstrating that expression of *kras*^{G12V} alone is associated
161 with low levels of cell death (Fig. 3a,b). However, the number of Annexin 5 fluorescent objects was
162 3.5-fold higher (5.2 puncta per 10^{-5} μm^3) in the livers of *ahctf1*$^{+/-}$*;tp53*$^{+/+}$*;TO(kras*^{G12V}*)*$^{T/+}$ larvae
163 demonstrating that the reduction in tumour burden caused by *ahctf1* heterozygosity is due, at least
164 in part, to an increase in cell death (Fig. 3a,b left two columns). These results were recapitulated when
165 the cleaved, (active form) of caspase 3 was used as an alternative marker of apoptosis (Supplementary
166 Fig. 4). That cell death in hyperplastic hepatocytes is largely dependent on Tp53 function was
167 demonstrated by negligible apoptosis in the livers of *ahctf1*$^{+/+}$*;tp53*$^{m/m}$*;TO(kras*^{G12V}*)*$^{T/+}$ larvae (Fig. 3a,b
168 right two columns). When this experiment was repeated on a heterozygous *ahctf1*$^{+/-}$ background, we
169 observed a 17.6-fold increase in the abundance of Annexin 5 fluorescent puncta compared to livers

170 on a WT *ahctf1* background. However, overall, there were significantly fewer Annexin 5 puncta in
171 heterozygous *ahctf1* hepatocytes on *tp53*$^{m/m}$ background compared to those expressing WT *tp53*.
172 Collectively, these data identify a novel synthetic lethal interaction between *kras*^{G12V} and one mutated
173 allele of *ahctf1* that is mediated, at least in part, by Tp53.

174 We showed that the elevated level of Tp53 protein observed in *ahctf1*$^{+/-}$*;TO(kras*^{G12V}*)*$^{T/+}$ livers,
175 compared to *ahctf1*$^{+/+}$*;TO(kras*^{G12V}*)*$^{T/+}$ livers (Fig. 2e,f), was transcriptionally active by the upregulated
176 (4.7-fold) mRNA expression of a canonical Tp53 target gene, *mdm2* (Fig. 3c). This prompted us to
177 quantify the mRNA expression levels of a suite of Bcl2 family genes that regulate intrinsic
178 (mitochondrial) apoptosis (Fig. 3c). Direct Tp53 transcriptional targets, *pmaip1* (aka *noxa*) and *bbc3*
179 (aka *puma*), were both upregulated by >6.5-fold in *ahctf1*$^{+/-}$*;tp53*$^{+/+}$*;TO(kras*^{G12V}*)*$^{T/+}$ livers compared to
180 *ahctf1*$^{+/+}$*;tp53*$^{+/+}$*;TO(kras*^{G12V}*)*$^{T/+}$ livers. mRNAs encoding the other BH3-only apoptosis effector
181 proteins, Bim, Bid, Bik and Bad, and the pro-apoptotic executioner protein, Bax were also increased in
182 *ahctf1*$^{+/-}$*;tp53*$^{+/+}$*;TO(kras*^{G12V}*)*$^{T/+}$ livers compared to *ahctf1*$^{+/+}$*;tp53*$^{+/+}$*;TO(kras*^{G12V}*)*$^{T/+}$ livers. Meanwhile,
183 transcripts encoding Bcl2 and Bclxl pro-survival proteins were significantly downregulated by *ahctf1*
184 heterozygosity. In the absence of Tp53 function, *ahctf1* heterozygosity still increased the expression
185 of these pro-apoptotic transcripts, albeit less markedly. All these data are consistent with induction
186 of Tp53 target genes playing a major role in the cell death response to *ahctf1* heterozygosity in
187 *kras*^{G12V}-expressing livers. Notwithstanding this, we observed some residual cell death concomitant
188 with reduced tumour burden in *ahctf1* heterozygotes, even in the absence of Tp53 function.

189 **_ahctf1_ heterozygosity restricts DNA replication in _TO(kras_^{G12V}_)_$^{T/+}$ hepatocytes**

190 To explore whether the reduction in liver enlargement we observe in *ahctf1*$^{+/-}$*;TO(kras*^{G12V}*)*$^{T/+}$ larvae
191 also involves impaired cell cycle progression, we used an EdU incorporation assay to identify cells in S
192 phase (Fig. 4a). We observed 32% EdU-positive cells in the enlarged livers of
193 *ahctf1*$^{+/+}$*;tp53*$^{+/+}$*;TO(kras*^{G12V}*)*$^{T/+}$ larvae and >20% EdU-positive cells (32% reduction) in the livers of
194 *ahctf1*$^{+/-}$*; tp53*$^{+/+}$*;TO(kras*^{G12V}*)*$^{T/+}$ larvae (Fig. 4b,c). In Tp53 deficient larvae, liver volume was markedly

195 increased as expected (Fig. 4b) and there was a doubling in the percentage of EdU-positive cells (63%
196 compared to 32%) (Fig. 4c). *ahctf1* heterozygosity reduced liver volume in both Tp53 proficient and
197 deficient larvae (Fig. 4b), consistent with Fig. 2, and reduced the percentage of EdU-positive cells in
198 both Tp53 proficient (22% compared to 32%) and Tp53 deficient larvae (53% compared to 63%) (Fig.
199 4c). These data indicate that the overall reduction in liver tumour burden we observe in response to
200 *ahctf1* heterozygosity is due to a combination of fewer cells undergoing DNA replication and more
201 cells undergoing apoptosis.

202 To investigate the molecular mechanisms underlying this observation, we performed RT-qPCR analysis
203 of the negative cell cycle regulators, *cdkn1a* and *cdkn2a/b* in the presence and absence of Tp53. We
204 found that *cdkn1a* and *cdkn2a/b*, encoding p21 and p16^{Ink4a} respectively, were upregulated in *ahctf1*$^{+/-}$
205 *;tp53*$^{+/+}$;*TO(kras*^{G12V}*)*$^{T/+}$ livers compared to *ahctf1*$^{+/+}$*;tp53*$^{+/+}$;*TO(kras*^{G12V}*)*$^{T/+}$ livers (Fig. 4d). For *cdkn1a*,
206 this response to *ahctf1* heterozygosity was partially dependent on intact Tp53 function. In contrast,
207 the level of *cdkn2a/b* mRNA expression was increased in response to *ahctf1* heterozygosity in
208 *tp53*$^{+/+}$*;TO(kras*^{G12V}*)*$^{T/+}$ livers, but there was no response to *ahctf1* heterozygosity in *tp53*$^{m/m}$ livers,
209 consistent with *cdkn2a/b* expression being regulated solely by Tp53.

210 To determine how *ahctf1* heterozygosity reduces tumour burden in the absence of Tp53, we
211 investigated the impact of *ahctf1* heterozygosity on the expression of *tp53* family members, *tp63* and
212 *tp73*. *tp63* and *tp73* mRNA expression levels were up-regulated by 3.0-fold and 2.3-fold, respectively,
213 in heterozygous *ahctf1*, *tp53*$^{+/+}$*;TO(kras*^{G12V}*)*$^{T/+}$ livers, compared to WT *ahctf1* livers. While *tp63* and
214 *tp73* transcripts were upregulated in the absence of *tp53* (*tp53*$^{m/m}$) for both *ahctf*1 genotypes, their
215 levels were significantly higher in *ahctf1* heterozygotes. Taken together, the data in Figs. 3 and 4
216 suggest that *ahctf1* heterozygosity constrains *kras*^{G12V}-driven hepatocyte hyperplasia and liver
217 enlargement by activating Tp53 transcriptional programs that induce cell cycle arrest and cell death.
218 Furthermore, the beneficial effect of *ahctf1* heterozygosity to reduce tumour burden persists in the
219 absence of functional Tp53, due to compensatory increases in the levels of *tp63* and *tp73*.

220 ***ahctf1* heterozygosity disrupts the abundance of nuclear pore complexes in *TO(kras^{G12V})$^{T/+}$***
221 **hepatocytes.**

222 To determine how *ahctf1* heterozygosity leads to Tp53 activation, we examined the integrity of some
223 of the essential processes in which the Elys protein plays a role. As depicted in Fig. 1, Elys fulfils many
224 distinct functions during the cell cycle. Starting with post-mitotic nuclear pore assembly (Fig. 1a), we
225 used Airyscan confocal laser-scanning microscopy to look at the abundance and distribution of NPCs
226 in thick sections of liver (200 μm) stained with an antibody (mAb414) that recognises FG-repeat Nups
227 (Nup358, 214, 153 and 62) in mature NPCs. Non-*kras^{G12V}* expressing hepatocytes exhibited fluorescent
228 puncta corresponding to NPCs at the nuclear rim with negligible staining in the cytoplasm, a pattern
229 that was unaffected by *ahctf1* genotype (Fig. 5a; left two columns). Upon induction of expression of
230 the *TO(kras^{G12V})$^{T/+}$* transgene, fluorescence intensity was markedly increased in the presence of
231 wildtype *ahctf1* (Fig 5a, third column) and there was an increase in the ratio of nuclear:cytoplasmic
232 staining (Fig 5b). However, fluorescence intensity at the nuclear rim was diminished in *ahctf1*
233 heterozygotes, concomitant with the appearance of puncta in the cytoplasm (Fig. 5a, fourth column;
234 arrows), leading to a 21% reduction in the ratio of nuclear:cytoplasmic fluorescence intensity (Fig. 5b).

235 To determine the abundance of NPCs, we analysed images acquired at the nuclear surface (Fig. 5c).
236 The pattern and density of fluorescent puncta observed at the nuclear surface of non-*kras^{G12V}*
237 expressing hepatocytes was not affected by *ahctf1* genotype (Fig. 5c; left two columns). The
238 expression of the *kras^{G12V}* transgene in the presence of wildtype *ahctf1* resulted in 59% more
239 fluorescent puncta/NPCs at the nuclear surface of hyperplastic hepatocytes, which was reduced by
240 20% in response to *ahctf1* heterozygosity (Fig. 5c, d; right two columns). Induced *kras^{G12V}* expression
241 also produced a 28% increase in nuclear volume compared to non-*kras^{G12V}* expressing cells (Fig. 5e),
242 and this increase was reduced to 13% by *ahctf1* heterozygosity. Together, these data indicate that
243 hyperplastic hepatocytes expressing the *kras^{G12V}* oncogene contain more abundant nuclear pores and
244 larger nuclei than their non-*kras^{G12V}* expressing counterparts, properties that are likely to enhance the
245 trafficking of mRNAs and proteins in and out of the nucleus to support the transcriptional and

246 translational needs of rapidly cycling cancer cells. However, *ahctf1* heterozygosity reduced NPC
247 density in *kras*^{G12V}-hepatocytes, potentially restricting the efficiency of nucleocytoplasmic trafficking.

248 **_ahctf1_ heterozygosity impairs mitotic spindle assembly and chromosome segregation in**
249 **_TO(kras_^{G12V}_)_$^{T/+}$ hepatocytes**

250 Next, we examined the impact of reduced Elys expression on spindle formation and chromosome
251 segregation (Fig. 1b). We assessed these features in cryosections of liver using α-tubulin and DAPI to
252 stain microtubules and chromatin, respectively. Metaphase cells in *ahctf1*$^{+/+}$*;TO(kras*^{G12V}*)*$^{T/+}$ livers
253 exhibited normal bipolar spindle formation followed by complete chromosome segregation during
254 anaphase (Fig. 6a). In contrast, metaphase cells in *ahctf1*$^{+/-}$*;TO(kras*^{G12V}*)*$^{T/+}$ hepatocytes displayed
255 abnormal multipolar spindles and misaligned chromosomes (Fig. 6b). Proper chromosome
256 segregation was disrupted with multiple anaphase bridges formed. While the distribution of cells
257 observed at different mitotic stages was similar in *ahctf1*$^{+/+}$ and *ahctf1*$^{+/-}$ hepatocytes (Fig. 6c), mitotic
258 abnormalities were observed in 50% of *ahctf1*$^{+/-}$*;TO(kras*^{G12V}*)*$^{T/+}$ hepatocytes during metaphase and
259 anaphase but not at all in *ahctf1*$^{+/+}$*;TO(kras*^{G12V}*)*$^{T/+}$ hepatocytes (Fig. 6d). Taken together, these data
260 suggest that hyperplastic hepatocytes require a full complement of *ahctf1* expression to maintain
261 proper cell division.

262 **_ahctf1_ heterozygosity causes DNA damage in _TO(kras_^{G12V}_)_$^{T/+}$ hepatocytes**

263 So far, our results demonstrate that a 50% decrease in *ahctf1* expression has multiple impacts in
264 *TO(kras*^{G12V}*)*$^{T/+}$ hepatocytes, including disrupted NPC assembly, impaired mitotic spindle assembly and
265 incomplete chromosome segregation, consistent with oncogene-induced stress. As several of these
266 defects can converge to produce DNA damage, we looked for evidence of DNA damage by staining
267 cryosections of liver with DAPI and γ-H2AX to mark DNA double-stranded breaks (Fig. 7a,b). We found
268 that only 1% of *ahctf1*$^{+/+}$*;TO(kras*^{G12V}*)*$^{T/+}$ hepatocyte nuclei were positive for γ-H2AX (Fig. 7c). This was
269 increased by 6-fold in *ahctf1*$^{+/-}$*;TO(kras*^{G12V}*)*$^{T/+}$ hepatocyte nuclei.

270 Collectively, these data show that the proper functioning of diverse cellular processes in hyperplastic
271 hepatocytes depends on wildtype levels of *ahctf1* expression. We show that heterozygous expression
272 of *ahctf1* in mutant Kras-fuelled cancer cells leads to multiple insufficiencies that combine to amplify
273 oncogene-induced stress and cause DNA damage, in so doing providing a stimulus to activate Tp53
274 and transcriptional programs that trigger cell cycle arrest and apoptosis.

275 **Combinatorial approaches can completely restrict *kras^{G12V}*-driven liver hyperplasia**

276 Having determined that heterozygous *ahctf1* mutation is effective in restricting *kras^{G12V}*-driven
277 hepatocyte hyperplasia and liver enlargement, we investigated the potential of targeting cancer via
278 another nucleoporin, Ranbp2, in our zebrafish model of HCC. RANBP2 (also known as NUP358) is a
279 major component of the cytoplasmic filaments of NPCs, where it functions in numerous transport
280 pathways. Like ELYS, RANBP2 also plays non-canonical roles outside of the NPC, including in mitotic
281 progression and the maintenance of genome integrity[28-30,31].

282 We identified our zebrafish *ranbp2* mutant in a transgene assisted ENU-mutagenesis screen for
283 mutations affecting endodermal organ morphogenesis[32] and showed, using whole genome
284 sequencing and homozygosity mapping[33,34], that the underlying mutation was a nonsense mutation in
285 *ranbp2* (Supplementary Fig. 5). Like several other mutants we identified in this screen[8,35,36], mutant
286 *ranbp2* larvae exhibit morphological deficiencies in proliferative compartments, including the
287 developing intestinal epithelium, craniofacial complex and eye (Supplementary Fig. 5).

288 We found that *ranbp2* heterozygosity alone or in combination with *ahctf1* heterozygosity did not
289 impact on liver volume in *2-CLiP* larvae (Fig. 8a,b). In *TO(kras^{G12V})$^{T/+}$* larvae, liver volume was increased
290 3.8-fold, as observed previously, and the excess liver volume was reduced by 38% and 13% by the
291 introduction of a single mutation in *ahctf1* and *ranbp2*, respectively (Fig. 8b). Remarkably, we found a
292 striking synergistic benefit of trans heterozygosity in *ranbp2$^{+/-}$;ahctf1$^{+/-}$;TO(kras^{G12V})$^{T/+}$* larvae, to the
293 extent that liver volume was no longer distinguishable from that of normal *2-CLiP* livers. These results
294 show that cancer cells are highly susceptible to combinatorial targeting of Nup function and that it

295 may be possible to exploit this vulnerability to produce highly beneficial outcomes without impacting
296 negatively on healthy tissues.

297 To examine this concept in a therapeutic context, we assessed the effect of Selinexor, a selective
298 inhibitor of nuclear export (SINE) in our *kras*^{G12V}-driven liver hyperplasia model. Selinexor is an XPO1
299 (exportin) inhibitor with FDA approval for the treatment of refractory or relapsed multiple myeloma
300 and diffuse large B-cell lymphoma and is in clinical trials for several other cancers, including HCC[37,38].
301 While we observed no reduction in liver volume in *2-CLiP* larvae exposed to 0.10-2.00 µM Selinexor
302 from 5 to 7 dpf (Fig. 8c,d) (Supplementary Fig. 6), *ahctf1*$^{+/+}$*;TO(kras*^{G12V}*)*$^{T/+}$ larvae exhibited a dose-
303 dependent reduction in liver volume when exposed to Selinexor. Strikingly, liver volume was reduced
304 even further in the context of *ahctf1* heterozygosity, such that at a 1.00 µM dose of Selinexor, *kras*^{G12V}-
305 driven hepatocyte hyperplasia was completely blocked and liver volume was indistinguishable from
306 that of normal, non-hyperplastic *2-CLiP* larvae (Fig. 8c,d). These results indicate that XPO1 inhibition
307 is an effective suppressor of growth and proliferation in our model of mutant Kras-driven HCC, and
308 that its impact can be reinforced by a concomitant reduction in Elys function.

309 We next examined whether there was any clinical rationale for developing Nup inhibitors for the
310 purpose of cancer treatment. We analysed the gene expression data of 372 HCC patients in the TCGA
311 liver hepatocellular carcinoma (LIHC) dataset collated in the cBioPortal for Cancer Genomics[39,40] for
312 *AHCTF1* and other genes encoding components of the NUP107-160 complex (Supplementary Table 3).
313 In a striking result, we found that the median overall survival of patients with high mRNA expression
314 of components of the NUP107-160 complex, including ELYS is 21.70 months, whereas the survival of
315 patients with low expression of mRNAs encoding NUP107-160 components is markedly extended to
316 81.73 months (Fig. 8e). Since the 372 samples in the LIHC dataset were profiled across 19 sequencing
317 plates that could cause batch effects and unwanted variation, we determined the integrity of this
318 result by performing ANOVA tests to assess the effects of individual sequencing plates on the
319 expression of genes encoding components of the NUP107-160 complex (Supplementary Fig. 7). These
320 analyses revealed that differences in gene expression observed between samples were largely

321 unaffected by unwanted variation between sequencing plates. This clinical observation supports our

322 proposition that ELYS and potentially other Nups would be useful targets for cancer treatment.

323

324 **DISCUSSION**

325 In this paper we show that *ahctf1* heterozygosity markedly reduces tumour burden in a genetically
326 engineered zebrafish model of HCC. Several factors indicate that this model provides a clinically
327 relevant platform for the study of human HCC and the discovery of new therapeutic strategies[24].
328 Firstly, RAS/RAF/MAPK signalling is almost always hyper-activated in human HCC[41]. Secondly, the
329 progressive accumulation of histopathologic features including irregular nuclei, cytoplasmic
330 vacuolation and increased vascularisation that are characteristic of tumour progression in HCC are
331 reproduced in the zebrafish model[42]. Thirdly, comparative transcriptomic analysis reveals that the
332 gene expression profile exhibited by oncogenic *kras*^{G12V} hepatocytes isolated from larval zebrafish
333 strongly resembles that of early-stage human HCC, with elevated expression of RAS/RAF/MAPK target
334 genes such as *FGFR4, ETV4, EPHA2, DUSP6* and *SPRY* and DNA damage response genes *GADD45B,*
335 *CCND1* and *H2AX1*[43].

336 Our results with this *in vivo* model of HCC compliment a growing body of evidence that carcinogenesis
337 places persistently high demands on essential cellular genes, including those required for proper
338 nuclear pore function, creating a vulnerability that may be therapeutically targeted without causing
339 adverse effects on normal tissue[44,45]. For example, Sakuma *et al*. used siRNAs targeting 28 out of 32
340 Nup genes, to reduce the abundance of mature NPCs in the human melanoma-derived cell line,
341 A375[44]. Focusing on two Nups exhibiting a severe reduction in NPC density, this study showed that
342 NUP160 and NUP93 are essential for NPC assembly and that inhibiting this process results in cell
343 death. Moreover, they found that cancer cells exhibited heightened susceptibility to inhibition of NPC
344 assembly compared to human pulmonary fibroblasts and a normal cell line derived from retinal
345 pigmental epithelium (RPE1), which instead underwent reversible cell cycle arrest. The differential
346 sensitivity between cancer cells and normal cells to NPC assembly inhibition is consistent with reports
347 that quiescent cells in normal tissues generally maintain low levels of Nup expression and may exist
348 for many years with the same set of assembled NPCs[46,47].

349 That *AHCTF1* might play a role in *RAS*-fuelled cancer cells was first indicated in a genome-wide RNAi
350 screen carried-out in human colorectal cancer-derived DLD1 cells[3]. Since then, a collection of genome-
351 wide CRISPR knockout screens has shown that *AHCTF1* is essential for the survival of 786/789 human
352 cancer cell lines[48,49] (Supplementary Table 3). While these data show that *AHCTF1* is indispensable for
353 virtually all cancer cell lines, *AHCTF1* expression is severely and irreversibly depleted in this *in vitro*
354 setting (>90%), and there is no read-out of how this degree of knockdown impacts on healthy cells.
355 We believe our *in vivo* experiments are more informative, not only because they show that a 50%
356 reduction in *ahctf1* gene dosage markedly reduces tumour burden but also because they show that
357 this is achieved without a detrimental impact on healthy cells.

358 Mutations in *TP53*, or amplification/overexpression of its negative regulators *MDM2*/*MDM4*, occur in
359 30% of HCC cases[50]. This is very relevant to our study because we show that a prominent response to
360 *ahctf1* heterozygosity in our *in vivo* HCC model is accumulation of DNA damage and activation of Tp53.
361 We therefore wondered whether the potential therapeutic effect of inhibiting ELYS function in a
362 clinical cancer setting would be diminished in tumours lacking functional TP53 protein. To address this
363 question, we studied the impact of *ahctf1* heterozygosity in our *in vivo* HCC model on a homozygous
364 *tp53* mutant background. We found that *ahctf1* heterozygosity still produced a 24% reduction in
365 tumour burden and induced cell death in the complete absence of Tp53 function, leading us to
366 consider whether the loss of Tp53 function was compensated for by increased *tp63* and/or *tp73*
367 expression. These genes encode Tp53 family proteins that share considerable structural homology
368 with Tp53, particularly within the DNA binding domain, and they can activate common and distinct
369 sets of target genes to produce cell cycle arrest, senescence and apoptosis[51,52]. For example, in
370 response to DNA damage, Tp63 induces senescence and apoptosis in the same way as Tp53, via
371 transcriptional induction of *cdkn1a*, *bbc3* and *pmaip1*[53]. We found that *ahctf1* heterozygosity
372 upregulated *tp63* and *tp73* expression by 3.0-fold and 2.3-fold, respectively, and that this was further
373 enhanced by homozygous *tp53* mutation. These results suggest a mechanism through which *ahctf1*
374 heterozygosity achieves a reduction in tumour burden in the absence of Tp53 function. Since *TP63*

375 and *TP73* are rarely mutated in cancer[54], we think that inhibition of ELYS function is likely to produce
376 a beneficial effect on tumour growth, even in patients harbouring *TP53* mutations.

377 Dysregulation of nucleocytoplasmic transport is a common feature in a broad spectrum of cancers,
378 usually arising from altered expression of nuclear pore components and/or nuclear transport
379 receptors[55]. For example, overexpression of POM121, a transmembrane NPC component, enhances
380 the nuclear import of the pro-proliferation transcription factors, E2F1, MYC and AR, and increases the
381 therapeutic resistance of prostate cancer[56]. Similarly, the nuclear transport receptor XPO1 is
382 frequently overexpressed in cancers, including HCC, and in this case leads to mis-localisation and
383 inactivation of tumour suppressor proteins[38,57]. As a result, numerous selective inhibitors of nuclear
384 export (SINEs) have been developed, including Selinexor (KPT-330), which has advanced through
385 clinical trials and received FDA approval for the treatment of relapsed or refractory multiple myeloma
386 and diffuse large B-cell lymphoma[37]. We found that Selinexor treatment in our zebrafish HCC model
387 produced a dose-dependent reduction in tumour burden. Moreover, this therapeutic effect was
388 strongly augmented by *ahctf1* heterozygosity, suggesting that new drugs targeting the ELYS protein
389 could be combined effectively with drugs that target nucleocytoplasmic transport. We also exploited
390 the genetic tractability of our zebrafish HCC model to show that trans heterozygosity of *ahctf1*, *ranbp2*
391 delivers a synergistic reduction in liver volume/tumour burden, bringing it back to the volume of non-
392 hyperplastic livers. Notably, non-*TO(kras^{G12V})* livers were completely unaffected by *ahctf1*, *ranbp2*
393 trans heterozygosity, indicating a three-way synthetic lethal interaction in cancer cells that may be
394 possible to recapitulate with combinatorial drug treatments.

395 The dynamic and diverse functions of ELYS require its binding to Nups and many other proteins,
396 including components of kinetochore and replicative licensing complexes, as well as binding to
397 chromatin in various states of condensation. The molecular topology of the ELYS protein and the
398 structural basis for its diverse protein-protein and protein-chromatin interactions are hitherto poorly
399 defined. Crystal structures of ELYS have shown that the β-propeller and α-helical domains in the N-
400 terminal half of the ELYS protein bind to NUP160, and cryo-electron microscopy reveals the

401 association of the ELYS C-terminal peptide with nucleosomes[21,58]. However, further high-resolution
402 structural characterization is required to advance our molecular understanding of the extent to which
403 discrete domains within the ELYS protein contribute to its various interactions, and to reveal
404 opportunities to inhibit such regions for the purpose of disabling ELYS function therapeutically. It is
405 possible that the topology of ELYS lacks features that would facilitate high affinity binding with small
406 drug-like molecules, as has been suggested for other Nups with scaffolding properties[44]. However,
407 rapidly emerging technological advances in drug development are likely to provide alternative
408 strategies to target the ELYS protein. For example, carefully controlled proteasomal degradation of
409 proteins that participate in the oncogenic process using proteolysis targeting chimeras (PROTACs) is a
410 rapidly advancing field in cancer therapy[59]. This approach depends on the availability of a ligand/probe
411 to direct the PROTAC to the targeted protein, but this need not be a druggable site of protein-protein
412 or protein-chromatin interaction, as is the case for small molecules designed to disrupt the function
413 of the protein. In parallel, emerging small molecule RNA-targeting technology is on course to permit
414 direct modulation of the abundance of specific RNA transcripts for a variety of clinical purposes[60]. In
415 summary, we believe our *in vivo* cancer studies provide a strong and feasible rationale for targeting
416 ELYS for the treatment of a broad spectrum of cancers and suggest potential avenues for effective
417 combinatorial treatments.

418

419 **MATERIALS AND METHODS**

420 **Zebrafish maintenance and strains**

421 Zebrafish were maintained at 28°C on a 12 h light/12 h dark cycle. The mutant lines *ahctf1*^{ti262} and
422 *tp53*$^{M214K/M214K}$ (also known as *tp53*$^{e7/e7}$ and referred to herein as *tp53*$^{m/m}$) have been described
423 previously[7,26]. Tg(*fabp10:dsRed, ela3l:GFP*)^{gz12}, hereafter referred to as *2-CLiP*, expresses dsRed in the
424 liver and GFP in the exocrine pancreas but carries no oncogenic transgenes or mutations[25]. The
425 Tg(*fabp10:rtTA2s-M2;TRE2:EGFP-kras*^{G12V})^{gz32} line referred to as *TO(kras*^{G12V}*)*$^{T/+}$ and the cell death
426 reporter line, Tg(*actb2:SEC-Hsa.ANXA5-mKate2,cryaa:mCherry*)^{uq24rp} were described previously[24,27].
427 The *ranbp2*^{s452} mutant line was generated in the Liver^{plus} ENU mutagenesis screen[32], and its genetic
428 and morphological characterization is presented in this paper.

429 **Inducing hepatocyte hyperplasia in transgenic zebrafish**

430 To induce *kras*^{G12V} expression, *TO(kras*^{G12V}*)*$^{T/+}$ embryos were treated with 20 µg/mL doxycycline
431 (Sigma, #D9891) at 2 dpf in E3 medium (5 mM NaCl, 0.17 mM KCl, 0.33 mM $CaCl_2$, 0.33 mM $MgSO_4$)
432 with 0.003% 1-Phenyl-2-thiourea (PTU; Sigma, #P7629) to suppress pigmentation. E3 medium was
433 changed at 5 dpf and fresh doxycycline (final conc. 20 µg/mL) added. For the Selinexor experiments,
434 the drug (final concentration 0.10-2.00 µM) (Karyopharm) or 0.001% DMSO (vehicle control) was
435 added at 5 dpf. Morphological and molecular analyses were performed at 7 dpf. To quantitate liver
436 volume, larvae were anaesthetized with benzocaine (200 mg/L) and mounted in 1% agarose. Image
437 acquisition was performed using an Olympus FVMPE- RS multiphoton microscope with a 25x objective
438 and Olympus FV30-SW software. Excitation wavelengths for GFP and RFP were 840 nm and 1100 nm,
439 respectively. For volumetric analysis of whole livers, z-stacks with step-size 2 µm, were imported into
440 ImageJ or Imaris software.

441

442 **Genotyping**

443 Genomic DNA (gDNA) was extracted from whole zebrafish larvae by incubation at 95°C in 50 µL of 50
444 mM sodium hydroxide (NaOH) for 20 min, followed by neutralization with 5 µL of 1 M Tris-HCl (pH
445 8.0). Primer sequences for genotyping are listed in Supplementary Table 1.

446 **mRNA expression analysis**

447 Total RNA was extracted from independent pools of micro-dissected zebrafish livers using the RNeasy
448 Micro Kit (QIAGEN, #74004). RNA integrity was assessed by a High Sensitivity RNA ScreenTape assay
449 (Agilent, #5067-5579) on a 2200 TapeStation. cDNA was generated from 1-10 µg RNA using the
450 Superscript III First Strand Synthesis System (Invitrogen, #18080051) and oligo(dT) priming according
451 to the manufacturer's instructions. RT-quantitative PCR (RT-qPCR) was performed using a SensiMix
452 SYBR kit (Bioline, #QT605-05) on an Applied Biosystems ViiATM7 Real-Time PCR machine. Expression
453 data were normalized by reference to *hrpt1*, *b2m* and *tbp*. LinRegPCR V11.0 was used for baseline
454 correction, PCR efficiency calculation and transcript quantification analysis[61]. Relative expression
455 levels were calculated by the $2^{-\Delta\Delta Ct}$ method and all results were expressed as the mean ± SEM of three
456 independent pools of biological replicates. Primer sequences are listed in Supplementary Table 2.

457 **Western blot analysis**

458 Pooled micro-dissected zebrafish livers were lysed in RIPA buffer (20mM Hepes, pH 7.9, 150mM NaCl,
459 1mM MgCl2, 1% NP40, 10mM NaF, 0.2mM Na3VO4, 10mM β-glycerol phosphate) supplemented with
460 cOmplete Proteinase Inhibitor (Roche, #11836170001) and PhosTOP phosphatase inhibitors (Roche,
461 #04906837001). Samples were incubated for 30 min on ice and the extracts cleared by centrifugation
462 at 13,000 rpm for 20 min at 4°C. The protein concentration of samples was determined by BCA protein
463 assay (Thermo Fisher Scientific, #23227). 25 µg of protein per lane were resolved on NuPAGE Novex
464 Bis-Tris 4-12% polyacrylamide gels (Invitrogen, #NP0321BOX) and transferred onto nitrocellulose
465 blotting membranes (Amersham Protran, #10600003). Membranes were blocked with 5% BSA in PBS
466 for 1 h at RT and incubated with primary antibodies 1:500 Anti-p53 (9.1) mouse mAb (Abcam,

467 #ab77813) overnight at 4°C and 1:1000 Anti-GAPDH (14C10) Rabbit mAb (Cell Signalling Technology,
468 #2118) for 1 h at RT. Secondary antibodies: Goat anti-mouse HRP (Dako, #P0447) and Goat anti-Rabbit
469 HRP (Dako, #P0448), were used at 1:5000 and incubated with membranes for 1 h at RT. Signals were
470 developed using Amersham ECL Western Blotting Detection Kit (Cytiva, # RPN2108) and imaged on a
471 Chemidoc Touch (Biorad). Relative protein quantitation was calculated based on normalized
472 integrated intensity.

473 **Cell death analysis**

474 To assess apoptosis, 7 dpf *TO(kras^{G12V});Annexin 5-mKate* zebrafish larvae were fixed in 4%
475 paraformaldehyde (PFA) overnight at 4°C and livers isolated by micro-dissection. Image acquisition
476 was performed using a Zeiss LSM 880 microscope with a 20x objective and ZEN software. Excitation
477 wavelengths for mKate and GFP were 560 nm and 900 nm, respectively. Liver volume was quantified
478 and 3D segmentation of Annexin 5-mKate signals were performed in ImageJ.

479 **Cell cycle analysis**

480 EdU incorporation was used to assess the percentage of cells in S phase of the cell cycle. Briefly, live
481 zebrafish larvae (7 dpf) were incubated at 28°C in 2 mM EdU (Invitrogen, #C10340) in E3 medium for
482 2 h followed by a further incubation in fresh E3 medium for 1 h. Larvae were euthanised using
483 benzocaine (1000 mg/L; Sigma, #PHR1158) prior to removal of the liver by micro-dissection. EdU
484 labelling was carried out using the Click-iT Edu Alexa Fluor 647 (AF647) imaging kit (Invitrogen,
485 #C10340), according to the manufacturer's instructions. The livers were co-stained with Hoechst
486 33342 (Thermofisher, #62249). Image acquisition was performed using an Olympus FVMPE-RS
487 multiphoton microscope with excitation wavelengths of 950 nm for Hoechst 33342 dye and 1160 nm
488 for AF647 (Thermofisher, #A21235). The number of Hoechst 33342 and EdU positive cells was
489 quantified using Arivis Vision4D software.

490 **Nuclear pore analysis**

491 Larvae fixed in 4% PFA overnight at 4°C were embedded in 4% low melting temperature agarose and
492 transverse sections collected at 200 µm intervals using a vibrating microtome (Leica VT 1000S).
493 Sections were blocked with 1% BSA in PBS/0.3% Triton X-100 and incubated with a 1:750 dilution of
494 mAb414 (Abcam, #ab24609) at 4°C overnight. Sections were then incubated with 1:500 anti-mouse
495 AF647 and Hoechst 33342 at room temperature for 1 h. Sections were mounted and imaged using a
496 Zeiss LSM880 Fast Airyscan Confocal microscope with a 63x objective. 3D segmentation of cells was
497 performed in ImageJ using EGFP signal for *TO(kras^{G12V})$^{T/+}$* larvae or F-actin stained with 1:200
498 rhodamine phalloidin for *TO(kras^{G12V})$^{+/+}$* larvae . An outline was drawn around the nuclear periphery
499 and segmented using the Hoechst signal. mAb414 fluorescence intensity was calculated for the
500 nuclear periphery and for the cytoplasm. NPC density was calculated by finding maxima for mAb414
501 at the nuclear surface of 5 nuclei per liver.

502 **Cryosectioning and immunofluorescence microscopy analysis**

503 Dissected livers were fixed in 4% PFA overnight at 4°C and washed with PBS/0.1% Tween 20 before
504 incubation in 30% sucrose in PBS overnight at 4°C. Livers were aligned in a tissue mould, embedded
505 in OCT and frozen on dry ice. The livers were sectioned at 10 µm intervals using a Thermofisher
506 Scientific Microm HM550 cryostat. Sections were washed with PBS before blocking with 10% FCS in
507 PBS/0.3% Triton X-100. Incubation with primary antibodies was performed at 4°C overnight, while
508 incubation with secondary antibodies was performed at room temperature for 1 h. Antibodies used
509 in this work were: 1:2000 α-Tubulin DM1A (CST, #3873), 1:1000 γ-H2AX (gift of James Amatruda),
510 1:250 cleaved caspase 3 (CST, #9664), 1:500 anti-rabbit AF647 (Thermofisher scientific, #A31573) and
511 1:500 anti-mouse AF647 (Thermofisher, #A21235). Prolong Diamond Antifade reagent with DAPI
512 (Thermofisher #P36962) was used for slide mounting. A Zeiss LSM880 Fast Airyscan Confocal
513 microscope with a 63x objective was used for image acquisition and ImageJ for image analysis.

514 **Statistical analysis**

515 Data are expressed as mean ± SEM unless indicated otherwise and the number of biological replicates
516 indicating samples from individual animals/livers, or pools of individual animals/livers for each
517 experiment are stated in the figure legends. P-values were calculated using Student's *t*-tests (two-
518 tailed, followed by Welch's correction) when comparing two groups, and by ANOVA followed by
519 Tukey's post-hoc test when comparing multiple groups. The effect of Selinexor treatment on liver
520 volume was analysed by linear regression, regressing liver volume against Selinexor concentration. All
521 analysis was performed using GraphPad Prism V7.03 (GraphPad software) and p-values ≤ 0.05 were
522 considered statistically significant.

523

ACKNOWLEDGEMENTS

The authors thank Tyson Blanch, Cameron Mackey, Elizabeth Grgacic and Bryan Ko (zebrafish husbandry), Ellen Tsui (histology), James Amatruda (rabbit polyclonal antibody to zebrafish γ-H2AX), Brendon Monahan and Leigh Coultas (insightful discussions).

COMPETING INTERESTS

The authors declare no competing financial interests.

ADDITIONAL INFORMATION

FUNDING

This work was funded by an Australian Government Research Training Program Scholarship and a WEHI Bridging Fellowship (to KM), the National Health and Medical Research Council of Australia (Grant 1024878 to JKH), Ludwig Cancer Research, a Victorian State Government Operational Infrastructure Support grant, and the Australian Government NHMRC Independent Research Institute Infrastructure Support Scheme.

AUTHORS' CONTRIBUTIONS

KM, KD, JKH conceived and designed the experiments; KM, KD, KS, BH, CS, GB, RM, ATP, TH, EO, DYRS, ZG, JKH developed the methodology; KM, KD, FG, LW, KS, BH, CS, GB, RM, ATP, JKH acquired and analysed the data; KM, KD and JKH wrote the manuscript; KD, JKH supervised the study; JKH acquired the funding.

DATA AVAILABILITY

The datasets generated and/or analysed during the current study are available in the cBioPortal Cancer Genomics database (http://www.cbioportal.org).

546 **REFERENCES**

547 1 Gao, S. & Lai, L. Synthetic lethality in drug development: the dawn is coming. *Future Med*
548 *Chem* **10**, 2129-2132, doi:10.4155/fmc-2018-0227 (2018).

549 2 Lord, C. J. & Ashworth, A. PARP inhibitors: Synthetic lethality in the clinic. *Science* **355**, 1152-
550 1158, doi:10.1126/science.aam7344 (2017).

551 3 Luo, J. *et al.* A genome-wide RNAi screen identifies multiple synthetic lethal interactions with
552 the Ras oncogene. *Cell* **137**, 835-848, doi:10.1016/j.cell.2009.05.006 (2009).

553 4 Wang, T. *et al.* Gene Essentiality Profiling Reveals Gene Networks and Synthetic Lethal
554 Interactions with Oncogenic Ras. *Cell* **168**, 890-903 e815, doi:10.1016/j.cell.2017.01.013
555 (2017).

556 5 Solimini, N. L., Luo, J. & Elledge, S. J. Non-oncogene addiction and the stress phenotype of
557 cancer cells. *Cell* **130**, 986-988, doi:10.1016/j.cell.2007.09.007 (2007).

558 6 Okita, K. *et al.* Targeted disruption of the mouse ELYS gene results in embryonic death at
559 peri-implantation development. *Genes Cells* **9**, 1083-1091, doi:10.1111/j.1365-
560 2443.2004.00791.x (2004).

561 7 Chen, J. N. *et al.* Mutations affecting the cardiovascular system and other internal organs in
562 zebrafish. *Development* **123**, 293-302 (1996).

563 8 de Jong-Curtain, T. A. *et al.* Abnormal nuclear pore formation triggers apoptosis in the
564 intestinal epithelium of elys-deficient zebrafish. *Gastroenterology* **136**, 902-911,
565 doi:10.1053/j.gastro.2008.11.012 (2009).

566 9 Davuluri, G. *et al.* Mutation of the zebrafish nucleoporin elys sensitizes tissue progenitors to
567 replication stress. *PLoS Genet* **4**, e1000240, doi:10.1371/journal.pgen.1000240 (2008).

568 10 Rasala, B. A., Orjalo, A. V., Shen, Z., Briggs, S. & Forbes, D. J. ELYS is a dual
569 nucleoporin/kinetochore protein required for nuclear pore assembly and proper cell
570 division. *Proc Natl Acad Sci U S A* **103**, 17801-17806, doi:10.1073/pnas.0608484103 (2006).

571 11 Gillespie, P. J., Khoudoli, G. A., Stewart, G., Swedlow, J. R. & Blow, J. J. ELYS/MEL-28
572 chromatin association coordinates nuclear pore complex assembly and replication licensing.
573 *Curr Biol* **17**, 1657-1662, doi:10.1016/j.cub.2007.08.041 (2007).
574 12 Franz, C. *et al.* MEL-28/ELYS is required for the recruitment of nucleoporins to chromatin
575 and postmitotic nuclear pore complex assembly. *EMBO Rep* **8**, 165-172,
576 doi:10.1038/sj.embor.7400889 (2007).
577 13 Beck, M. & Hurt, E. The nuclear pore complex: understanding its function through structural
578 insight. *Nat Rev Mol Cell Biol* **18**, 73-89, doi:10.1038/nrm.2016.147 (2017).
579 14 Hodgson, B., Li, A., Tada, S. & Blow, J. J. Geminin becomes activated as an inhibitor of
580 Cdt1/RLF-B following nuclear import. *Curr Biol* **12**, 678-683, doi:10.1016/s0960-
581 9822(02)00778-9 (2002).
582 15 Kuhn, T. M., Pascual-Garcia, P., Gozalo, A., Little, S. C. & Capelson, M. Chromatin targeting of
583 nuclear pore proteins induces chromatin decondensation. *J Cell Biol* **218**, 2945-2961,
584 doi:10.1083/jcb.201807139 (2019).
585 16 Guttinger, S., Laurell, E. & Kutay, U. Orchestrating nuclear envelope disassembly and
586 reassembly during mitosis. *Nat Rev Mol Cell Biol* **10**, 178-191, doi:10.1038/nrm2641 (2009).
587 17 Chatel, G. & Fahrenkrog, B. Nucleoporins: leaving the nuclear pore complex for a successful
588 mitosis. *Cell Signal* **23**, 1555-1562, doi:10.1016/j.cellsig.2011.05.023 (2011).
589 18 Mishra, R. K., Chakraborty, P., Arnaoutov, A., Fontoura, B. M. & Dasso, M. The Nup107-160
590 complex and gamma-TuRC regulate microtubule polymerization at kinetochores. *Nat Cell*
591 *Biol* **12**, 164-169, doi:10.1038/ncb2016 (2010).
592 19 Orjalo, A. V. *et al.* The Nup107-160 nucleoporin complex is required for correct bipolar
593 spindle assembly. *Mol Biol Cell* **17**, 3806-3818, doi:10.1091/mbc.e05-11-1061 (2006).
594 20 Yokoyama, H. *et al.* The nucleoporin MEL-28 promotes RanGTP-dependent gamma-tubulin
595 recruitment and microtubule nucleation in mitotic spindle formation. *Nat Commun* **5**, 3270,
596 doi:10.1038/ncomms4270 (2014).

597 21 Kobayashi, W. *et al.* Structural and biochemical analyses of the nuclear pore complex
598 component ELYS identify residues responsible for nucleosome binding. *Commun Biol* **2**, 163,
599 doi:10.1038/s42003-019-0385-7 (2019).
600 22 Bilokapic, S. & Schwartz, T. U. Molecular basis for Nup37 and ELY5/ELYS recruitment to the
601 nuclear pore complex. *Proc Natl Acad Sci U S A* **109**, 15241-15246,
602 doi:10.1073/pnas.1205151109 (2012).
603 23 Rasala, B. A., Ramos, C., Harel, A. & Forbes, D. J. Capture of AT-rich chromatin by ELYS
604 recruits POM121 and NDC1 to initiate nuclear pore assembly. *Mol Biol Cell* **19**, 3982-3996,
605 doi:10.1091/mbc.E08-01-0012 (2008).
606 24 Chew, T. W. *et al.* Crosstalk of Ras and Rho: activation of RhoA abates Kras-induced liver
607 tumorigenesis in transgenic zebrafish models. *Oncogene* **33**, 2717-2727,
608 doi:10.1038/onc.2013.240 (2014).
609 25 Korzh, S. *et al.* Requirement of vasculogenesis and blood circulation in late stages of liver
610 growth in zebrafish. *BMC Dev Biol* **8**, 84, doi:10.1186/1471-213X-8-84 (2008).
611 26 Berghmans, S. *et al.* tp53 mutant zebrafish develop malignant peripheral nerve sheath
612 tumors. *Proc Natl Acad Sci U S A* **102**, 407-412, doi:10.1073/pnas.0406252102 (2005).
613 27 Hall, T. E. *et al.* Cellular rescue in a zebrafish model of congenital muscular dystrophy type
614 1A. *NPJ Regen Med* **4**, 21, doi:10.1038/s41536-019-0084-5 (2019).
615 28 Joseph, J., Liu, S. T., Jablonski, S. A., Yen, T. J. & Dasso, M. The RanGAP1-RanBP2 complex is
616 essential for microtubule-kinetochore interactions in vivo. *Curr Biol* **14**, 611-617,
617 doi:10.1016/j.cub.2004.03.031 (2004).
618 29 Salina, D., Enarson, P., Rattner, J. B. & Burke, B. Nup358 integrates nuclear envelope
619 breakdown with kinetochore assembly. *J Cell Biol* **162**, 991-1001,
620 doi:10.1083/jcb.200304080 (2003).

621 30 Hashizume, C., Kobayashi, A. & Wong, R. W. Down-modulation of nucleoporin
622 RanBP2/Nup358 impaired chromosomal alignment and induced mitotic catastrophe. *Cell*
623 *Death Dis* **4**, e854, doi:10.1038/cddis.2013.370 (2013).
624 31 Vecchione, L. *et al.* A Vulnerability of a Subset of Colon Cancers with Potential Clinical Utility.
625 *Cell* **165**, 317-330, doi:10.1016/j.cell.2016.02.059 (2016).
626 32 Ober, E. A., Verkade, H., Field, H. A. & Stainier, D. Y. Mesodermal Wnt2b signalling positively
627 regulates liver specification. *Nature* **442**, 688-691, doi:10.1038/nature04888 (2006).
628 33 Leshchiner, I. *et al.* Mutation mapping and identification by whole-genome sequencing.
629 *Genome Res* **22**, 1541-1548, doi:10.1101/gr.135541.111 (2012).
630 34 Voz, M. L. *et al.* Fast homozygosity mapping and identification of a zebrafish ENU-induced
631 mutation by whole-genome sequencing. *PLoS One* **7**, e34671,
632 doi:10.1371/journal.pone.0034671 (2012).
633 35 Boglev, Y. *et al.* Autophagy induction is a Tor- and Tp53-independent cell survival response
634 in a zebrafish model of disrupted ribosome biogenesis. *PLoS Genet* **9**, e1003279,
635 doi:10.1371/journal.pgen.1003279 (2013).
636 36 Markmiller, S. *et al.* Minor class splicing shapes the zebrafish transcriptome during
637 development. *Proc Natl Acad Sci U S A* **111**, 3062-3067, doi:10.1073/pnas.1305536111
638 (2014).
639 37 Jans, D. A., Martin, A. J. & Wagstaff, K. M. Inhibitors of nuclear transport. *Curr Opin Cell Biol*
640 **58**, 50-60, doi:10.1016/j.ceb.2019.01.001 (2019).
641 38 Zheng, Y. *et al.* KPT-330 inhibitor of XPO1-mediated nuclear export has anti-proliferative
642 activity in hepatocellular carcinoma. *Cancer Chemother Pharmacol* **74**, 487-495,
643 doi:10.1007/s00280-014-2495-8 (2014).
644 39 Cerami, E. *et al.* The cBio cancer genomics portal: an open platform for exploring
645 multidimensional cancer genomics data. *Cancer Discov* **2**, 401-404, doi:10.1158/2159-
646 8290.CD-12-0095 (2012).

647 40 Gao, J. *et al.* Integrative analysis of complex cancer genomics and clinical profiles using the
648 cBioPortal. *Sci Signal* **6**, pl1, doi:10.1126/scisignal.2004088 (2013).
649 41 Calvisi, D. F. *et al.* Ubiquitous activation of Ras and Jak/Stat pathways in human HCC.
650 *Gastroenterology* **130**, 1117-1128, doi:10.1053/j.gastro.2006.01.006 (2006).
651 42 Zheng, W. *et al.* Xmrk, kras and myc transgenic zebrafish liver cancer models share
652 molecular signatures with subsets of human hepatocellular carcinoma. *PLoS One* **9**, e91179,
653 doi:10.1371/journal.pone.0091179 (2014).
654 43 Huo, X. *et al.* Transcriptomic analyses of oncogenic hepatocytes reveal common and
655 different molecular pathways of hepatocarcinogenesis in different developmental stages
656 and genders in kras(G12V) transgenic zebrafish. *Biochem Biophys Res Commun* **510**, 558-
657 564, doi:10.1016/j.bbrc.2019.02.008 (2019).
658 44 Sakuma, S. *et al.* Inhibition of Nuclear Pore Complex Formation Selectively Induces Cancer
659 Cell Death. *Cancer Discov* **11**, 176-193, doi:10.1158/2159-8290.CD-20-0581 (2021).
660 45 Beck, M., Schirmacher, P. & Singer, S. Alterations of the nuclear transport system in
661 hepatocellular carcinoma - New basis for therapeutic strategies. *J Hepatol* **67**, 1051-1061,
662 doi:10.1016/j.jhep.2017.06.021 (2017).
663 46 D'Angelo, M. A., Raices, M., Panowski, S. H. & Hetzer, M. W. Age-dependent deterioration of
664 nuclear pore complexes causes a loss of nuclear integrity in postmitotic cells. *Cell* **136**, 284-
665 295, doi:10.1016/j.cell.2008.11.037 (2009).
666 47 Toyama, B. H. *et al.* Identification of long-lived proteins reveals exceptional stability of
667 essential cellular structures. *Cell* **154**, 971-982, doi:10.1016/j.cell.2013.07.037 (2013).
668 48 Dempster, J. M. *et al.* Extracting Biological Insights from the Project Achilles Genome-Scale
669 CRISPR Screens in Cancer Cell Lines. doi:10.1101/720243 (2019).
670 49 Meyers, R. M. *et al.* Computational correction of copy number effect improves specificity of
671 CRISPR-Cas9 essentiality screens in cancer cells. *Nat Genet* **49**, 1779-1784,
672 doi:10.1038/ng.3984 (2017).

673 50 Zucman-Rossi, J., Villanueva, A., Nault, J. C. & Llovet, J. M. Genetic Landscape and
674 Biomarkers of Hepatocellular Carcinoma. *Gastroenterology* **149**, 1226-1239 e1224,
675 doi:10.1053/j.gastro.2015.05.061 (2015).
676 51 Levrero, M. *et al.* The p53/p63/p73 family of transcription factors: overlapping and distinct
677 functions. *J Cell Sci* **113 (Pt 10)**, 1661-1670 (2000).
678 52 Suh, E. K. *et al.* p63 protects the female germ line during meiotic arrest. *Nature* **444**, 624-
679 628, doi:10.1038/nature05337 (2006).
680 53 Kerr, J. B. *et al.* DNA damage-induced primordial follicle oocyte apoptosis and loss of fertility
681 require TAp63-mediated induction of Puma and Noxa. *Mol Cell* **48**, 343-352,
682 doi:10.1016/j.molcel.2012.08.017 (2012).
683 54 Dotsch, V., Bernassola, F., Coutandin, D., Candi, E. & Melino, G. p63 and p73, the ancestors
684 of p53. *Cold Spring Harb Perspect Biol* **2**, a004887, doi:10.1101/cshperspect.a004887 (2010).
685 55 Kau, T. R., Way, J. C. & Silver, P. A. Nuclear transport and cancer: from mechanism to
686 intervention. *Nat Rev Cancer* **4**, 106-117, doi:10.1038/nrc1274 (2004).
687 56 Rodriguez-Bravo, V. *et al.* Nuclear Pores Promote Lethal Prostate Cancer by Increasing
688 POM121-Driven E2F1, MYC, and AR Nuclear Import. *Cell* **174**, 1200-1215 e1220,
689 doi:10.1016/j.cell.2018.07.015 (2018).
690 57 Hill, R., Cautain, B., de Pedro, N. & Link, W. Targeting nucleocytoplasmic transport in cancer
691 therapy. *Oncotarget* **5**, 11-28, doi:10.18632/oncotarget.1457 (2014).
692 58 Bilokapic, S. & Schwartz, T. U. Structural and functional studies of the 252 kDa nucleoporin
693 ELYS reveal distinct roles for its three tethered domains. *Structure* **21**, 572-580,
694 doi:10.1016/j.str.2013.02.006 (2013).
695 59 Ocana, A. & Pandiella, A. Proteolysis targeting chimeras (PROTACs) in cancer therapy.
696 *Journal of experimental & clinical cancer research : CR* **39**, 189, doi:10.1186/s13046-020-
697 01672-1 (2020).

698 60 Mukherjee, H. *et al.* PEARL-seq: A Photoaffinity Platform for the Analysis of Small Molecule-
699 RNA Interactions. *ACS Chem Biol* **15**, 2374-2381, doi:10.1021/acschembio.0c00357 (2020).
700 61 Ruijter, J. M. *et al.* Amplification efficiency: linking baseline and bias in the analysis of
701 quantitative PCR data. *Nucleic Acids Res* **37**, e45, doi:10.1093/nar/gkp045 (2009).
702

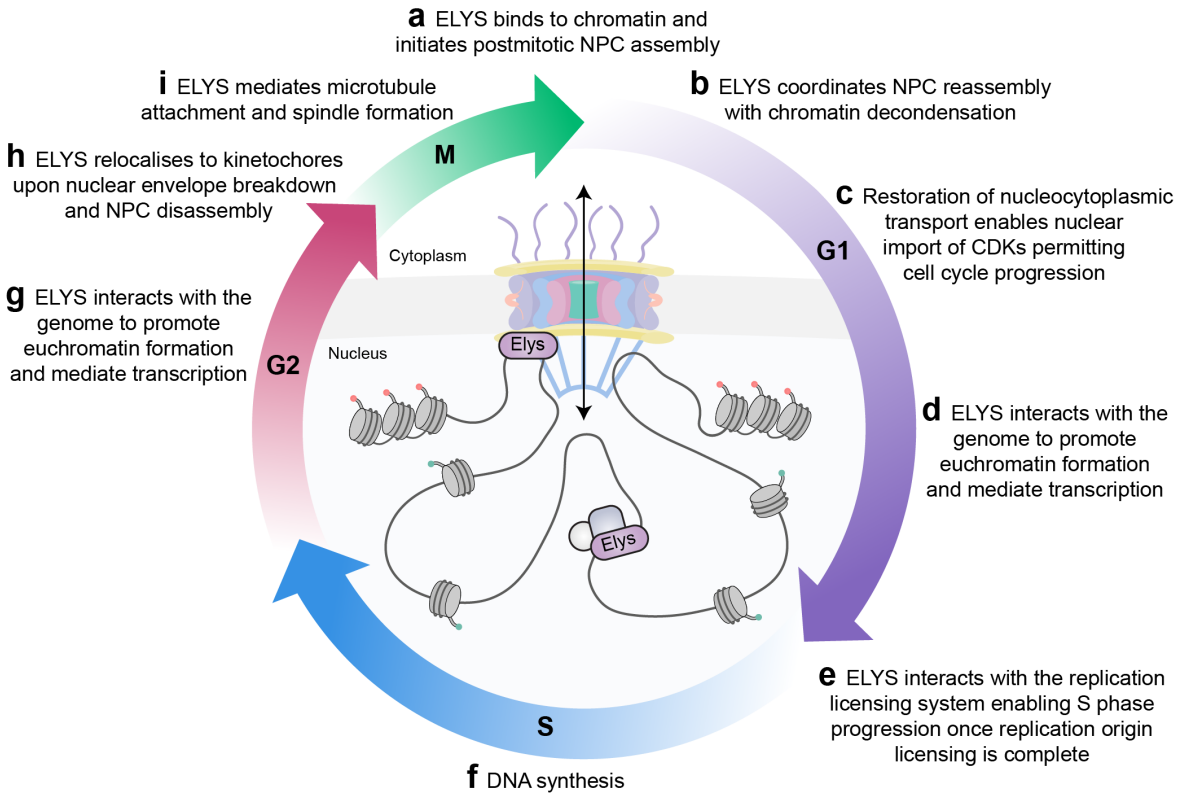

Fig. 1 Elys plays critical roles at several stages of the cell cycle.

Elys is a central player in multiple diverse cellular processes far beyond its canonical role in nuclear pore re-assembly at the end of mitosis **(a, b)**. **c.** Elys restores nucleocytoplasmic trafficking allowing import of cyclin-dependent kinases (CDKs) required for cell cycle progression. **d-g.** Elys plays an active role in genome regulation through its direct interactions with components of large molecular machineries including chromatin remodellers such as PBAP that favour transcription and the MCM2-7 components of the DNA replication origin licensing system. **h.** After cell growth in G2, the nuclear envelope breaks down and NPCs are disassembled upon entry into mitosis. **i.** Elys relocalizes to kinetochores where it contributes to microtubule attachment and spindle formation.

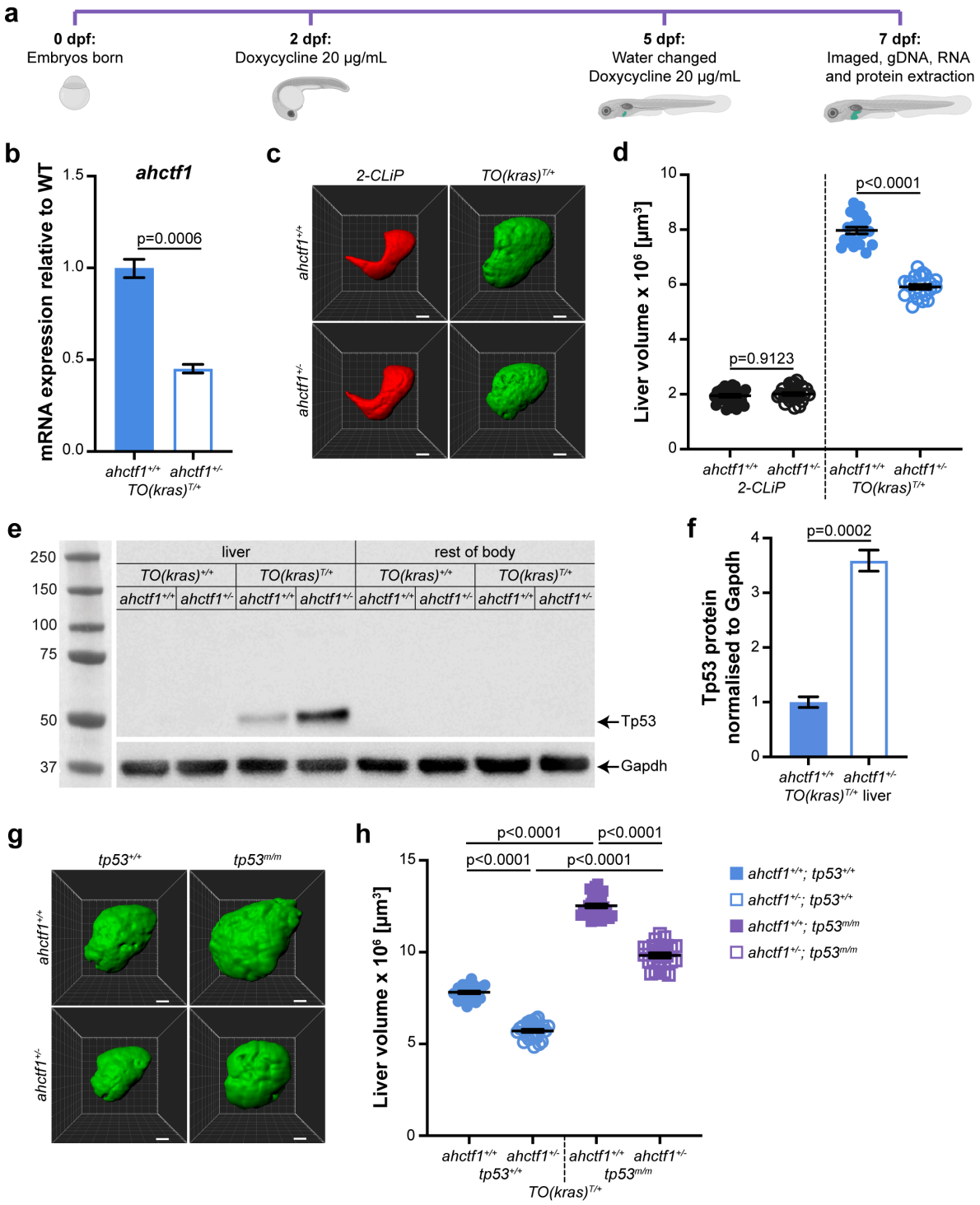

Fig. 2 *ahctf1* heterozygosity reduces liver volume in a zebrafish *kras*^{G12V}-driven model of hepatocellular carcinoma in both Tp53 proficient and deficient larvae.

a. Protocol for doxycycline induction of *TO(kras*^{G12V}*)*$^{T/+}$ expression in developing zebrafish larvae. **b.** RT-qPCR analysis of *ahctf1* mRNA levels in pooled micro-dissected livers (n=3 biological replicates). **c.** Representative three-dimensional reconstructions of *2-CLiP* and *TO(kras*^{G12V}*)*$^{T/+}$ livers of the indicated

720 *ahctf1* genotype. Scale bar 25 µm. **d.** Impact of *ahctf1* heterozygosity on liver volume in *2-CLiP* and
721 *TO(kras^{G12V})$^{T/+}$* larvae (n≥20). **e.** Representative western blot of Tp53 protein signals in lysates of
722 *TO(kras^{G12V})$^{T/+}$* larvae of the indicated *ahctf1* genotype. **f.** Quantification of Tp53 protein levels
723 normalised by reference to the Gapdh loading control (n=3 independent experiments). **g.**
724 Representative three-dimensional reconstructions of *TO(kras^{G12V})$^{T/+}$* livers of the indicated *ahctf1* and
725 *tp53* genotypes. Scale bar 25 µm. **h.** Impact of *ahctf1* heterozygosity and homozygous *tp53* mutation
726 on liver volume in *2-CLiP* and *TO(kras^{G12V})$^{T/+}$* larvae (n≥20). Data are expressed as mean ± SEM.
727 Significance was calculated using a Student's t-test or one-way ANOVA with Tukey's multiple
728 comparisons test.

729

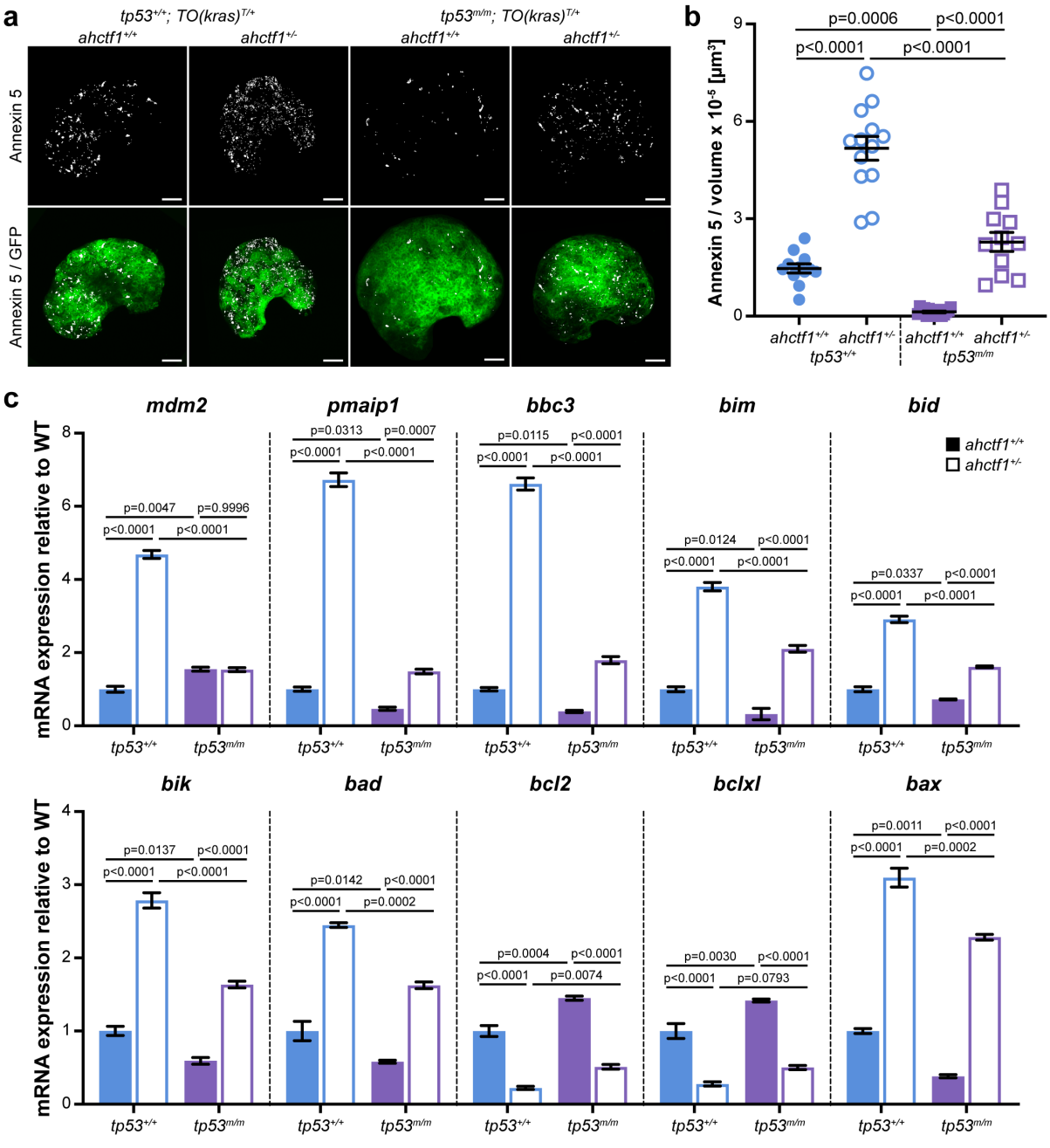

Fig. 3 *ahctf1* heterozygosity increases cell death in *TO(kras^{G12V})$^{T/+}$* hepatocytes in both Tp53 proficient and deficient larvae.

a. Representative maximum intensity projection images of Annexin 5-mKate fluorescence (white puncta), indicating cells undergoing apoptosis in *TO(kras^{G12V})$^{T/+}$* livers of the indicated *ahctf1* and *tp53* genotypes. Scale bar 25 µm. **b.** Quantification of the density of Annexin 5 fluorescent foci in *TO(kras^{G12V})$^{T/+}$* livers of the indicated *ahctf1* and *tp53* genotypes (n≥11). **c.** RT-qPCR analysis of the specified mRNAs in *TO(kras^{G12V})$^{T/+}$* micro-dissected livers of the indicated *ahctf1* and *tp53* genotypes

738 (n=3 biological replicates). Data are expressed as mean ± SEM. Significance was calculated using a one-

739 way ANOVA with Tukey's multiple comparisons test.

740

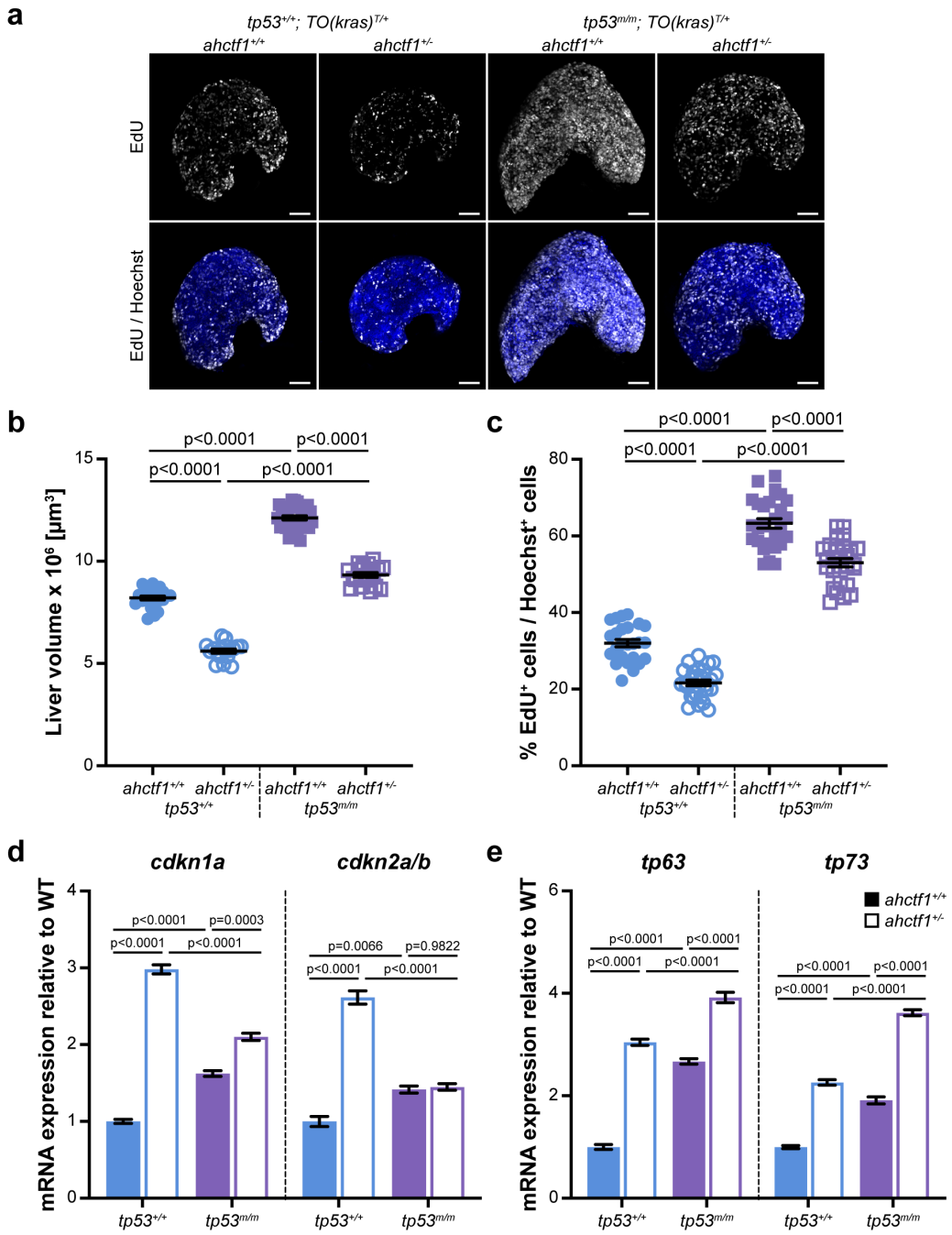

741

742 **Fig. 4 *ahctf1* heterozygosity restricts DNA replication in *TO(kras^{G12V})$^{T/+}$* hepatocytes.**

743 **a.** Representative maximum intensity projection images of EdU incorporation (white puncta) into
744 *TO(kras^{G12V})$^{T/+}$* livers of the indicated *ahctf1* and *tp53* genotypes. Scale bar 25 µm. **b.** Impact of *ahctf1*
745 heterozygosity and homozygous *tp53* mutation on liver volume in *2-CLiP* and *TO(kras^{G12V})$^{T/+}$* larvae
746 (n≥17). **c.** Quantification of the percentage of EdU positive nuclei per Hoechst 33342 positive nuclei
747 (n≥25). **d.** RT-qPCR analysis of mRNA expression of the cell cycle regulators, *cdkn1a* and *cdkn2a/b* and

748 **e.** *tp63* and *tp73* in *TO(kras^{G12V})$^{T/+}$* micro-dissected livers of the indicated *ahctf1* and *tp53* genotypes

749 (n=3 biological replicates). Data are expressed as mean ± SEM. Significance was assessed using a one-

750 way ANOVA with Tukey's multiple comparisons test.

751

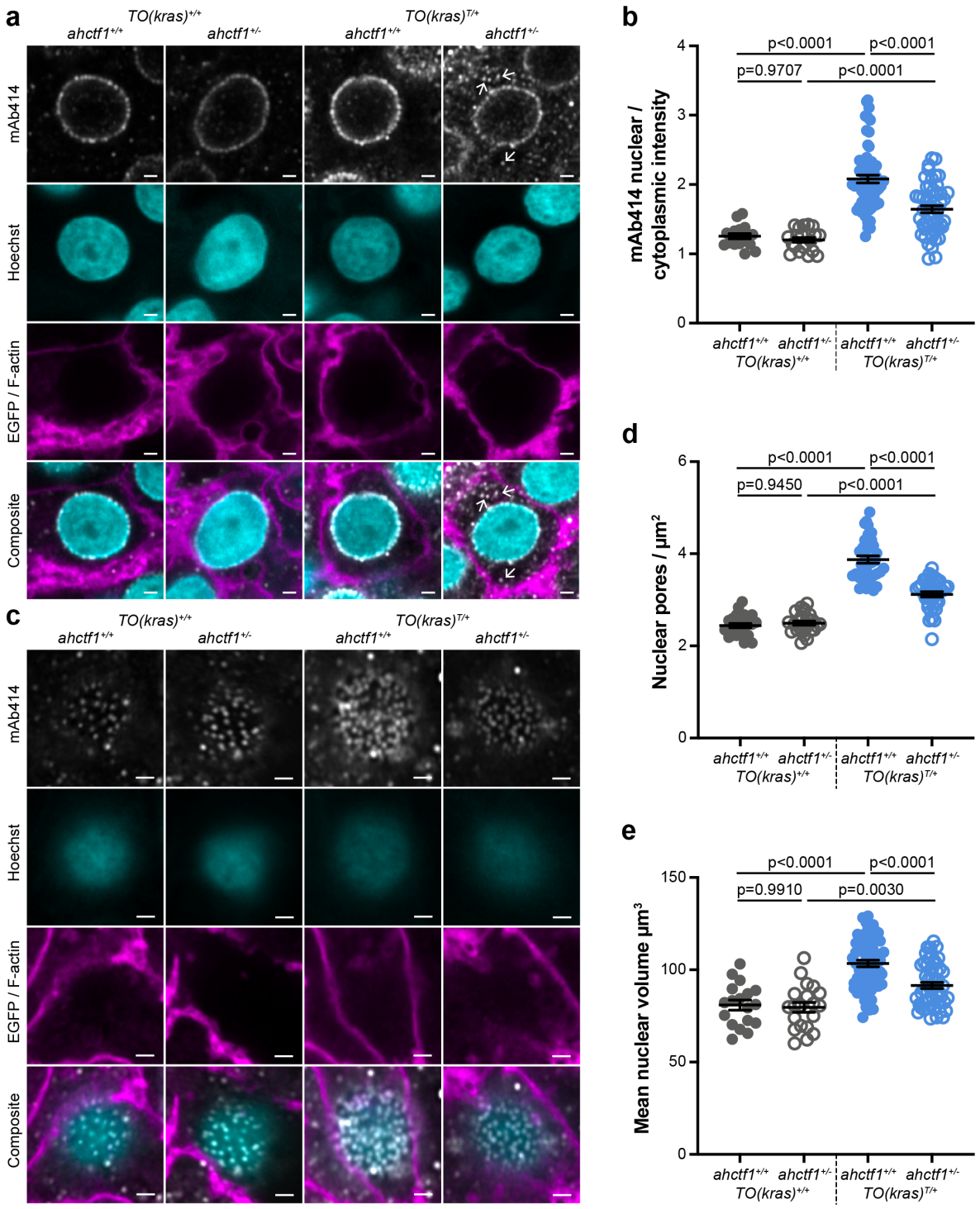

Fig. 5 *ahctf1* heterozygosity disrupts nuclear pore complexes in *TO(kras^{G12V})$^{T/+}$* hepatocytes.

a. Representative Airyscan imaging of liver sections stained with mAb414 (white) marking FG-Nups, Hoechst 33342 (cyan) marking DNA, and rhodamine phalloidin (magenta) marking the F-actin cytoskeleton in non-*TO(kras^{G12V})*-expressing cells or EGFP-Kras^{G12V} (magenta) marking the cell membrane in *TO(kras^{G12V})*-expressing cells of the indicated *ahctf1* and *TO(kras^{G12V})* genotypes. Arrows

758 in right hand panel point to mAb414/FG-nucleoporin staining in the cytoplasm. Scale bar 2 µm. **b.**
759 Quantification of mean nuclear/cytoplasmic fluorescence intensity of mAb414 staining after 3D
760 segmentation and morphological filtering of nuclear and cytoplasmic areas (n>18). **c.** Representative
761 Airyscan images of mAb414 staining at the nuclear surface of sections of the indicated *ahctf1* and
762 *TO(kras^{G12V})* genotype. Scale bar 1 µm**. d.** Quantification of nuclear pore density (n≥25). **e.**
763 Quantification of nuclear volume (n≥25). Data are expressed as mean ± SEM. Significance was assessed
764 using a one-way ANOVA with Tukey's multiple comparisons test.

765

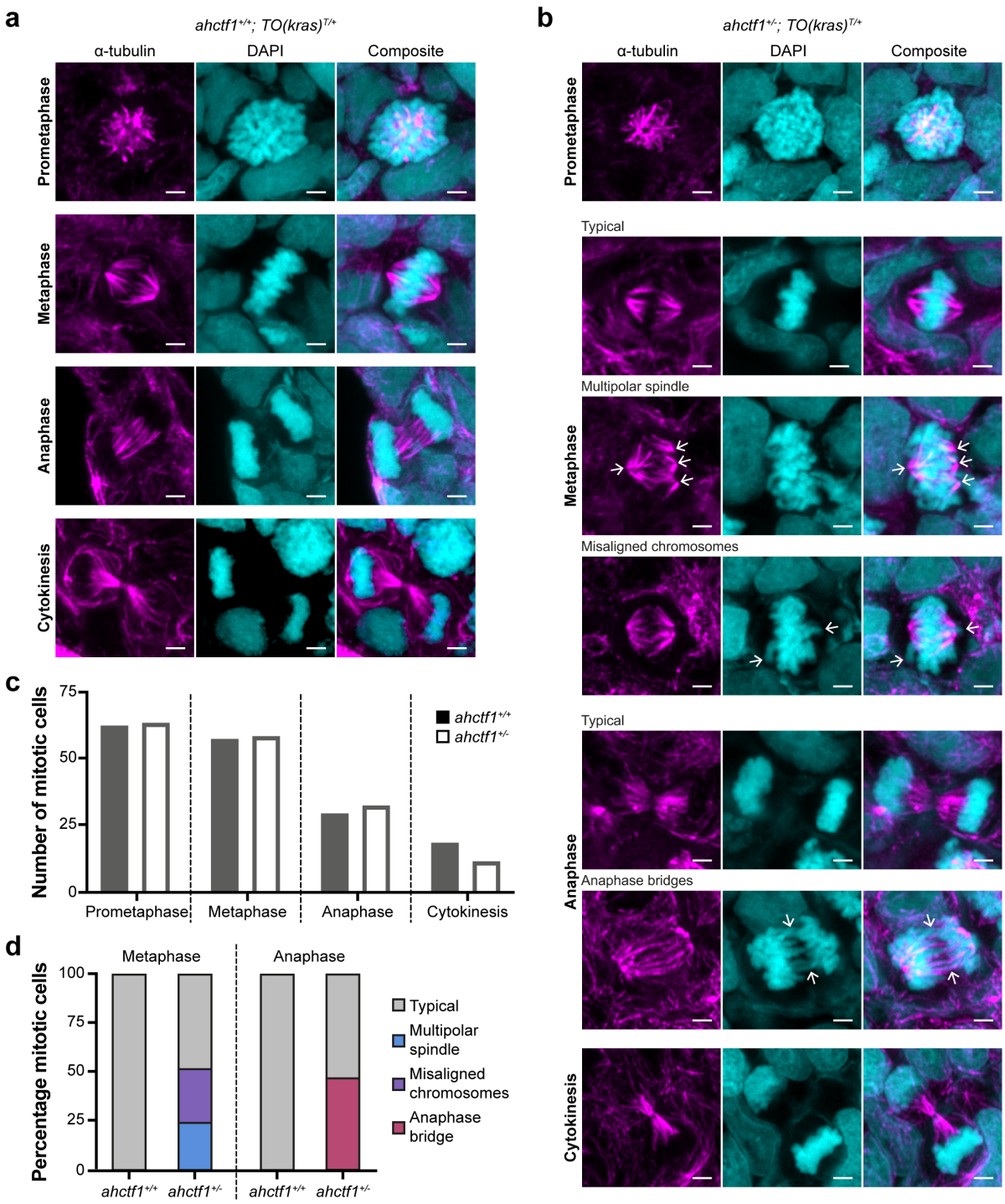

766

767 **Fig. 6 *ahctf1* heterozygosity impairs mitotic spindle assembly and chromosome segregation in**

768 ***TO(kras^{G12V})$^{T/+}$* hepatocytes.**

769 **a.** Representative Airyscan imaging of liver cryosections stained with α-tubulin antibody (magenta)

770 marking spindle microtubules and DAPI (cyan) marking DNA in mitotic cells of *TO(kras^{G12V})$^{T/+}$* larvae on

771 a wildtype *ahctf1$^{+/+}$* background. **b.** Mitotic cells in liver cryosections of *TO(kras^{G12V})$^{T/+}$* larvae on a

772 heterozygous *ahctf1*$^{+/-}$ background exhibit multiple defects, including multipolar spindles, misaligned
773 chromosomes and anaphase bridges (arrows). Scale bar 2 µm. **c.** Distribution of cells observed at
774 different mitotic stages (n=92 livers, 326 mitotic cells) **d.** Quantification of the percentage of mitotic
775 hepatocytes exhibiting an aberrant phenotype (n=14-57).

776

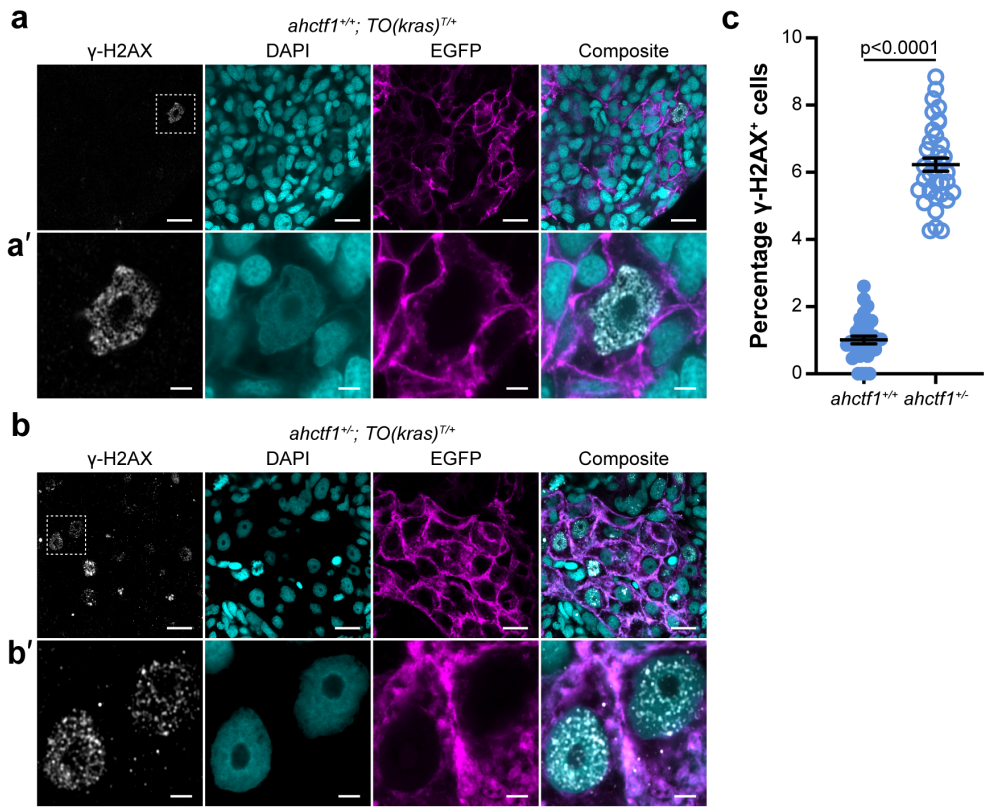

Fig. 7 *ahctf1* heterozygosity leads to accumulation of DNA double-strand breaks in *TO(kras^{G12V})$^{T/+}$* hepatocytes.

a. Representative Airyscan imaging of cryosections of liver from *ahctf1$^{+/+}$;TO(kras^{G12V})$^{T/+}$* larvae stained with γ-H2AX antibody (white) marking DNA double-strand breaks, DAPI (cyan) marking DNA and EGFP-Kras^{G12V} (magenta) marking the cell membrane. Scale bar 5 µm. **a'.** Inset of γ-H2AX positive nuclei in *ahctf1$^{+/+}$;TO(kras^{G12V})$^{T/+}$* hepatocytes. Scale bar 2 µm. **b.** Representative images of cryosections of liver from *ahctf1$^{+/-}$;TO(kras^{G12V})$^{T/+}$* larvae. Scale bar 5 µm. **b'.** Inset of γ-H2AX positive nuclei in cryosections of liver from *ahctf1$^{+/-}$;TO(kras^{G12V})$^{T/+}$* larvae. Scale bar 2 µm. **c.** Quantification of the percentage of hepatocytes positive for γ-H2AX (n≥31). Data are expressed as mean ± SEM. Significance was calculated using a Student's t-test.

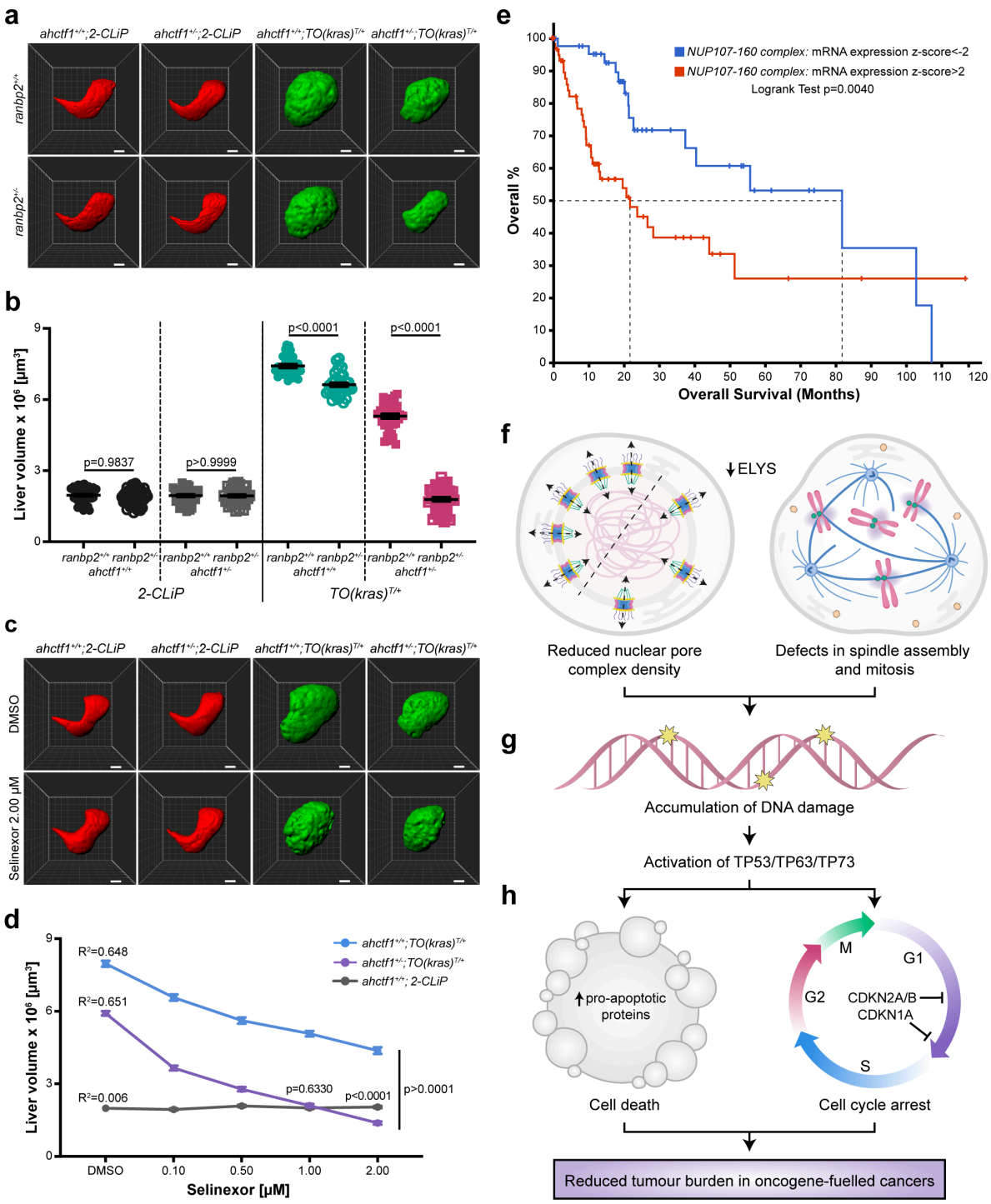

Fig. 8 Combined approaches completely restrict *kras*^{G12V}-driven liver hyperplasia.

a. Representative three-dimensional reconstructions of livers from *2-CLiP* and *TO(kras*^{G12V}*)*$^{T/+}$ larvae of the indicated *ahctf1* and *ranbp2* genotypes. Scale bar 25 µm. **b.** Impact of *ahctf1* heterozygosity and *ranbp2* heterozygosity on liver volume in *2-CLiP* and *TO(kras*^{G12V}*)*$^{T/+}$ larvae (n≥30). Significance was calculated using a one-way ANOVA with Tukey's multiple comparisons test. **c.** Representative three-

795 dimensional reconstructions of *TO(kras^{G12V})$^{T/+}$* livers of the indicated *ahctf1* genotype treated with
796 DMSO or 2.00 µM Selinexor from 5-7 dpf. **d.** Dose-dependent impact of Selinexor treatment (0.10-
797 2.00 µM) on liver volume in *2-CLiP* (grey), *ahctf1$^{+/+}$;TO(kras^{G12V})$^{T/+}$* (blue) and *ahctf1$^{+/-}$;TO(kras^{G12V})$^{T/+}$*
798 (purple) larvae (n≥20). Data are expressed as mean ± SEM. Significance was calculated by linear
799 regression analysis. **e.** Overall survival of HCC patients with mRNA expression z-scores >2 for one or
800 more Nup107-160 complex components (red line; 63 cases); median overall survival 21.70 months.
801 Overall survival of HCC patients with mRNA expression z-scores <-2 for one or more Nup107-160
802 complex components (blue line; 45 cases); median overall survival 81.73 months. Data from the TCGA
803 LIHC dataset (total 372 samples) available in the cBioPortal for Cancer Genomics. **f.** Schematic
804 depiction of two of the processes disrupted by mild depletion of Elys protein. **g.** Accumulation of DNA
805 damage and activation of Tp53 transcription programs. **h**. Cell death and cell cycle arrest of
806 hyperproliferative oncogene-expressing cancer cells.